

Testing the Cosmological Principle with CatWISE Quasars: A Bayesian Analysis of the Number-Count Dipole

Lawrence Dam^{1,2,*}, Geraint F. Lewis^{1,†} & Brendon J. Brewer³

¹*Sydney Institute for Astronomy, School of Physics, A28, The University of Sydney, NSW 2006, Australia*

²*Département de Physique Théorique and Center for Astroparticle Physics, Université de Genève, 24 quai Ernest-Ansermet, 1211 Genève 4, Switzerland*

³*Department of Statistics, The University of Auckland, Private Bag 92019, Auckland 1142, New Zealand*

Accepted XXX. Received YYY; in original form ZZZ

ABSTRACT

The Cosmological Principle, that the Universe is homogeneous and isotropic on sufficiently large scales, underpins the standard model of cosmology. However, a recent analysis of 1.36 million infrared-selected quasars has identified a significant tension in the amplitude of the number-count dipole compared to that derived from the CMB, thus challenging the Cosmological Principle. Here we present a Bayesian analysis of the same quasar sample, testing various hypotheses using the Bayesian evidence. We find unambiguous evidence for the presence of a dipole in the distribution of quasars with a direction that is consistent with the dipole identified in the CMB. However, the amplitude of the dipole is found to be 2.7 times larger than that expected from the conventional kinematic explanation of the CMB dipole, with a statistical significance of 5.7σ . To compare these results with theoretical expectations, we sharpen the Λ CDM predictions for the probability distribution of the amplitude, taking into account a number of observational and theoretical systematics. In particular, we show that the presence of the Galactic plane mask causes a considerable loss of dipole signal due to a leakage of power into higher multipoles, exacerbating the discrepancy in the amplitude. By contrast, we show using probabilistic arguments that the source evolution of quasars improves the discrepancy, but only mildly so. These results support the original findings of an anomalously large quasar dipole, independent of the statistical methodology used.

Key words: cosmology: large-scale structure of universe — cosmology: cosmic background radiation — cosmology: observations — quasars: general — galaxies: active

1 INTRODUCTION

The Cosmological Principle, the idea that the Universe is spatially homogeneous and isotropic when viewed at sufficiently large scales, underlies the use of Friedmann–Lemaître–Robertson–Walker (FLRW) world models in the standard concordance cosmology, Λ CDM. In these models there exist ideal observers for whom their view is an isotropic universe, such that in this ‘cosmic rest frame’ the CMB appears maximally isotropic (Maartens 2011). Any observer moving with velocity \mathbf{v} relative to this frame will observe a dipole anisotropy in the CMB temperature, $\Delta T/T \approx \boldsymbol{\beta} \cdot \hat{\mathbf{n}}$, where $\boldsymbol{\beta} = \mathbf{v}/c$ and $\hat{\mathbf{n}}$ is the direction of observation (Stewart & Sciamia 1967; Peebles & Wilkinson 1968). The fact that the CMB dipole as observed from in the heliocentric frame (which is about a hundred times larger than the primary anisotropies) is conventionally taken as evidence that the solar system is moving with speed (Planck Collaboration et al. 2020a)

$$v = (369.825 \pm 0.070) \text{ km s}^{-1} \quad (1)$$

towards

$$(l, b) = (264^\circ.021 \pm 0^\circ.009, 48^\circ.253 \pm 0^\circ.004), \quad (2)$$

relative to the CMB rest frame.

To test whether the CMB dipole has a genuine kinematic origin, Ellis & Baldwin (1984) proposed a simple consistency test using the number counts of radio sources on the sky: Given an isotropic distribution of sources, forming a background of uniform emission, our putative velocity should induce in the number counts a dipole anisotropy of the amplitude and direction expected by equation (1), *if the kinematic interpretation is correct*. Supposing a population of radio sources with identical flux density spectra $S \propto \nu^{-\alpha}$ (where ν is the frequency and α the spectral index), and integral source count above flux density threshold S_* given by $dN(> S_*)/d\Omega \propto S_*^{-x}$, Ellis & Baldwin (1984) showed that the number counts across the sky exhibits a dipole anisotropy $\Delta N/N = \mathbf{d}_k \cdot \hat{\mathbf{n}}$ with

$$\mathbf{d}_k = [2 + x(1 + \alpha)]\boldsymbol{\beta}. \quad (3)$$

This is the *kinematic dipole*. Here $\boldsymbol{\beta} = \mathbf{v}/c$, where \mathbf{v} is the velocity of the heliocentric frame relative to the ‘matter rest frame’, the frame in which the radio sources are observed at rest. Unless we have reason to expect, as in the standard model, that the matter rest frame coincides with the CMB rest frame, there is no *a priori* reason that the velocity in equation (3) is the same as the velocity in equation (1).

* E-mail: lawrence.dam@unige.ch

† E-mail: geraint.lewis@sydney.edu.au (GFL)

Conversely, the agreement of these two velocities then provides an indirect check on the Cosmological Principle (for a recent appraisal on its observational status, see [Aluri et al. 2023](#)).

In performing this check, one important advantage is that \mathbf{d}_k is independent of cosmological assumptions; in principle, \mathbf{d}_k arises from special-relativistic considerations, namely, the aberration and Doppler effects. In particular, for $\beta = 370 \text{ km s}^{-1}/c \approx 1.23 \times 10^{-3}$, and typical values $x \simeq 1$, $\alpha \simeq 1$, one expects a dipole of amplitude $d_k \simeq 5 \times 10^{-3}$, that is, we expect a 0.5% enhancement in the number counts towards the boost apex. Since this is a small effect, a precise measurement of it requires good sky coverage and number density.

In practice, Ellis and Baldwin’s test will be contaminated by the gravitational clustering of sources. Radio sources are tracers of large-scale structure, which, when integrated along the line of sight, produces an intrinsic anisotropy in the number counts. Thus, in addition to the kinematic dipole (3), we also have a *clustering dipole*, \mathbf{d}_c . The observed dipole is thus the combination of the kinematic and clustering dipole. Unlike \mathbf{d}_k , modelling \mathbf{d}_c from first principles does require cosmological assumptions. An interpretation of any dipole measurement needs to consider the impact of source clustering, as the amplitude of \mathbf{d}_c may be significant if the source population is relatively local. In any case, the expected amplitude d_c and its probability distribution, can be predicted from theory, as we show in this work.

The measurement of the radio dipole (and other matter dipoles) has seen a range of results from a variety of methods and data. Using radio sources from the NRAO VLA Sky Survey (NVSS; [Condon et al. 1998](#)) and a low-order spherical-harmonic fit, [Blake & Wall \(2002\)](#) reported one of the first measurements of the radio dipole, finding broad agreement with the CMB expectation (though with moderately large uncertainties). More recent measurements ([Singal 2011](#); [Gibelyou & Huterer 2012](#); [Rubart & Schwarz 2013](#); [Colin et al. 2017](#); [Bengaly et al. 2018](#)) have called on other surveys, including 2MASS, 2MRS, BATSE gamma-ray bursts, SUMSS ([Mauch et al. 2003](#)), WENSS ([Rengelink et al. 1997](#)) and TGSS; a detailed summary can be found in [Siewert, Schmidt-Rubart & Schwarz \(2021\)](#). These results provide further support for a larger-than-expected dipole broadly aligned with CMB. (Though see [Darling \(2022\)](#) who finds agreement with the CMB in both amplitude and direction using data from VLASS ([Lacy et al. 2020](#)) and RACS ([McConnell et al. 2020](#)) catalogues).

Recently, [Secrest et al. \(2021b\)](#), hereafter S21 provided one of the strongest challenges to the kinematic interpretation. As with previous results (with a direction consistent with the CMB) the amplitude was found to be discrepant by a factor of two (i.e. larger than expected). On the basis of simulations, the null hypothesis (kinematic origin) was rejected at a high statistical significance of 4.9σ . This determination was enabled by a large sample of quasars selected from the CatWISE2020 catalogue ([Marocco et al. 2021](#)) based on the all-sky Wide-field Infrared Survey Explorer (WISE; [Wright et al. 2010](#)). After applying a conservative Galactic plane cut, this sample consisted of 1.36 million quasars covering about 50% of the sky. With a favourable redshift distribution mitigating against contamination from a clustering dipole, the CatWISE quasar sample is ideal for carrying out the Ellis and Baldwin test.

Given the implications of such a discrepancy that challenge the basis of the standard model, it is worth reanalysing the sample of S21. We will however take a different statistical approach. Using a novel likelihood for the observed counts on the sky, we will present a Bayesian analysis of the source-count map for several parametric models. In brief, in reaching the same qualitative conclusions as S21 we demonstrate that the anomalous dipole amplitude is robust to

methodological differences of analysis. To assess the tension with Λ CDM, we give a first-principles comparison between our posterior probability distribution and the theoretical prior, refining the *a priori* predictions for the CatWISE dipole. In the process, we will investigate a number of systematics (e.g. masking, contamination from clustering, shot noise, source evolution) on the likely values of the amplitude, and the extent to which the discrepancy can be resolved. The layout of this paper is as follows. In Section 2 we outline the data sample and our approach, with the results of our analysis presented in Section 2.4. In Section 3 we compute the Λ CDM prior for the probability distribution of the dipole’s amplitude in the realistic case of partial-sky coverage. We present our conclusions in Section 4. A number of appendices present the details of the theoretical analysis undertaken in this paper.

2 BAYESIAN ANALYSIS

2.1 CatWISE quasar sample

For the purposes of this study, we employ an identical sample of quasars as presented by S21 ([Secrest et al. 2021a](#)). This is a flux-limited, all-sky sample consisting of 1,355,352 quasars selected from the CatWISE2020 catalogue ([Marocco et al. 2021](#)), a dataset derived from the infrared survey WISE ([Wright et al. 2010](#)) and NEOWISE ([Mainzer et al. 2014](#)), predominantly at $3.4 \mu\text{m}$ (*W1*) and $4.6 \mu\text{m}$ (*W2*). The S21 sample was obtained from a magnitude cut $9 < W1 < 16.4$, with AGN selected using the colour criterion $W1 - W2 \geq 0.8$ ([Stern et al. 2012](#)); masking was applied to the Galactic plane ($|b| < 30^\circ$), bright sources, poor-quality photometry, and image artefacts. The spectral indices α in *W1* band were measured for each source by power-law fits using both bands. In this sample, 99% of sources are at $z > 0.1$, while 61% are at $z > 1$; the mean redshift is 1.2.

In determining the presence of a dipole structure in the resultant quasar sample, we first binned the counts over the sky to determine their density. To achieve this, `healpy` (a Python implementation of HEALPix; [Górski et al. 2005](#); [Zonca et al. 2019](#)) was used to determine equal area pixels over the sky. For this study, $N_{\text{side}} = 64$, which corresponds to a total number of pixels of 49,152, each with an area of 0.83 square degrees. The total number of unmasked pixels is $n_{\text{pix}} = 23,972$, and the pixelized map analysed in this work is shown in Fig. 1.

2.2 Parametric model and likelihood

The expected number density of quasars in direction $\hat{\mathbf{n}}$ is given to a good approximation by the dipolar modulation (i.e. the sum of the monopole and dipole moments)

$$\frac{dN}{d\Omega}(\hat{\mathbf{n}}) = \bar{N}(1 + \mathbf{d} \cdot \hat{\mathbf{n}}), \quad (4)$$

where $\hat{\mathbf{n}}$ is the direction of observation, \bar{N} is the mean number density on the sky, and $\mathbf{d} \cdot \hat{\mathbf{n}}$ is the dipole. This equation forms the basis of our analysis. In practice, there are a number of systematics to be considered. In particular, S21 identified a scanning pattern bias in the CatWISE2020 sample that varies linearly away from the ecliptic equator, such that there is a decrease of source density of $\sim 7\%$ at the ecliptic poles. To allow for this possibility we introduce a biasing term of the form

$$f_{\text{ecl}}(\hat{\mathbf{n}}) \equiv 1 - \Upsilon_{\text{ecl}} c_{\text{ecl}} |b_{\text{ecl}}(\hat{\mathbf{n}})|, \quad (5)$$

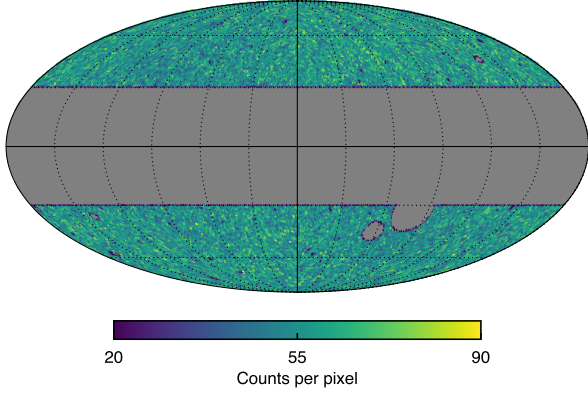


Figure 1. Mollweide map ($N_{\text{side}} = 64$) of the number-count density of the S21 quasar sample. Here the Galactic-plane cut removes $|b| < 30^\circ$. The mean number count is 57.4 per unmasked pixel, corresponding to a surface density of 69.2 quasars per square degree.

where the slope $c_{\text{ecl}} = 7.4 \times 10^{-4}$ was determined by S21 through a linear fit, and $b_{\text{ecl}}(\hat{\mathbf{n}})$ is the ecliptic latitude. We introduced Y_{ecl} , a nuisance parameter which exactly recovers the S21 correction when $Y_{\text{ecl}} = 1$, and corresponds to no ecliptic bias when $Y_{\text{ecl}} = 0$. With the inclusion of the ecliptic bias, the expected number of quasars in a HEALPIX pixel at $\hat{\mathbf{n}}$ is given by the parametric model

$$\lambda(\hat{\mathbf{n}}) = \Omega_{\text{pix}} \int_{\text{ecl}} \frac{dN}{d\Omega}(\hat{\mathbf{n}}), \quad (6)$$

where Ω_{pix} is the pixel area.

The counting statistics within each pixel motivates a likelihood of Poisson form, with mean varying from pixel to pixel due to the expected dipolar modulation. Hence, given the expected number of quasars $\lambda_i = \lambda(\hat{\mathbf{n}}_i)$ in the i th pixel, the probability of observing N_i quasars in that pixel is

$$p(N_i | \theta) = \frac{\lambda_i^{N_i} e^{-\lambda_i}}{N_i!}. \quad (7)$$

The likelihood of obtaining number counts $N_1, N_2, \dots, N_{n_{\text{pix}}}$ (the data \mathcal{D}) is therefore

$$\mathcal{L}(\theta; \mathcal{D}) = \prod_{i=1}^{n_{\text{pix}}} p(N_i | \theta), \quad (8)$$

where θ is the set of free parameters, and the product is taken over all n_{pix} unmasked pixels. In this work $\theta = \{\bar{N}, D, l, b, Y_{\text{ecl}}\}$, where $D \equiv |\mathbf{d}|$ is the dipole amplitude, l, b are the Galactic coordinates of \mathbf{d} (and \bar{N} and Y_{ecl} were described above).

One advantage of our Bayesian approach over other approaches often used is uncertainty quantification. This is a routine task once the posteriors are sampled, and yields an internal measure of the uncertainty (no simulations are required). Furthermore, the posterior can be directly compared with the distribution we expect from theory (Section 3). Indeed, previous estimates of the dipole are largely based on constructing estimators; see, e.g. Siewert et al. (2021) and references therein. However, in the situation where all cells have high occupancy number, the Poisson likelihood converges to a Gaussian, with both mean and variance equal to λ_i . In this limit we can derive from equation (7) the maximum-likelihood estimator of the dipole, which is equivalent (up to some normalisation) to the quadratic estimator commonly used. (With $N_{\text{side}} = 64$ we have about 57 sources per pixel, so we are well within this regime.) Although we will only extract the monopole and dipole, we note that the likelihood (8)

Table 1. Marginal likelihoods for the various models considered. Note that Z is increasing from M_0 to M_8 .

Model	Description	$\ln(Z)$
M_0	Null (no dipole)	-87707.67
M_1	Amplitude fixed to CMB; no bias	-87654.43
M_2	Amplitude and direction fixed to CMB; no bias	-87652.04
M_3	Direction fixed to CMB; no bias	-87625.43
M_4	All parameters free, except no bias	-87624.18
M_5	Amplitude fixed to CMB	-87473.38
M_6	Amplitude and direction fixed to CMB	-87472.77
M_7	Direction fixed to CMB	-87445.27
M_8	All parameters free	-87444.17

also retains complete information in the pixelized map, including of higher multipoles.

2.3 Hypotheses considered

For the purposes of this study, several differing hypotheses were considered and compared.

- M_0 : Taken to be the null hypothesis, this assumes that there is no dipole or ecliptic bias in the CatWISE sample, and only has a single free parameter, \bar{N} . D and Y_{ecl} are fixed at zero.

- M_1 : The dipole's amplitude is precisely that of the CMB but its direction may differ from that of the CMB. No ecliptic bias is assumed, so $Y_{\text{ecl}} = 0$.

- M_2 : This assumes that a dipole is present and has the same magnitude and direction as that observed in the CMB. For this, the amplitude is fixed to $D_{\text{CMB}} = 0.0072$, whilst the direction is fixed at $(l, b) = (264^\circ.021, 48^\circ.253)$. Again, \bar{N} is treated as a free parameter and no ecliptic bias is assumed ($Y_{\text{ecl}} = 0$).

- M_3 : Again, this assumes that a dipole is present, and is aligned with the CMB. However, the amplitude of the dipole term, D is treated as a free parameter, as is \bar{N} . The direction is fixed at $(l, b) = (264^\circ.021, 48^\circ.253)$, and no ecliptic bias is assumed ($Y_{\text{ecl}} = 0$).

- M_4 : Here, the presence of a dipole is assumed, but its amplitude and direction, D, l and b are taken as free parameters, as is \bar{N} . The ecliptic bias, Y_{ecl} , is again assumed to be zero.

Models M_1, M_2, M_3, M_4 were repeated (as M_5, M_6, M_7, M_8 , respectively) but with the ecliptic bias Y_{ecl} treated as a free parameter. These models are summarised in Table 1.

2.4 Posterior exploration

With given model M_i and data \mathcal{D} , the posterior probability distribution of obtaining the set of parameters θ is by Bayes' theorem

$$p(\theta | \mathcal{D}) = \mathcal{L}(\theta; \mathcal{D}) p(\theta) / Z, \quad (9)$$

where $p(\theta)$ is the prior and $Z \equiv \int d\theta \mathcal{L}(\theta; \mathcal{D}) p(\theta)$ is the marginal likelihood, or Bayesian evidence. We explored the posterior using the DNest4 sampler (Diffusive Nested Sampling; Brewer & Foreman-Mackey 2018), allowing a determination of the posterior distributions, but also providing the marginal likelihood. This allows an effective comparison of the competing hypotheses based on how well they predicted the data, marginalised over the parameter space of each model.

For the purposes of this study, the following priors were adopted. For the mean number count $\bar{N} \Omega_{\text{pix}}$ a uniform distribution between 40 and 60 was chosen. A uniform distribution was also adopted for

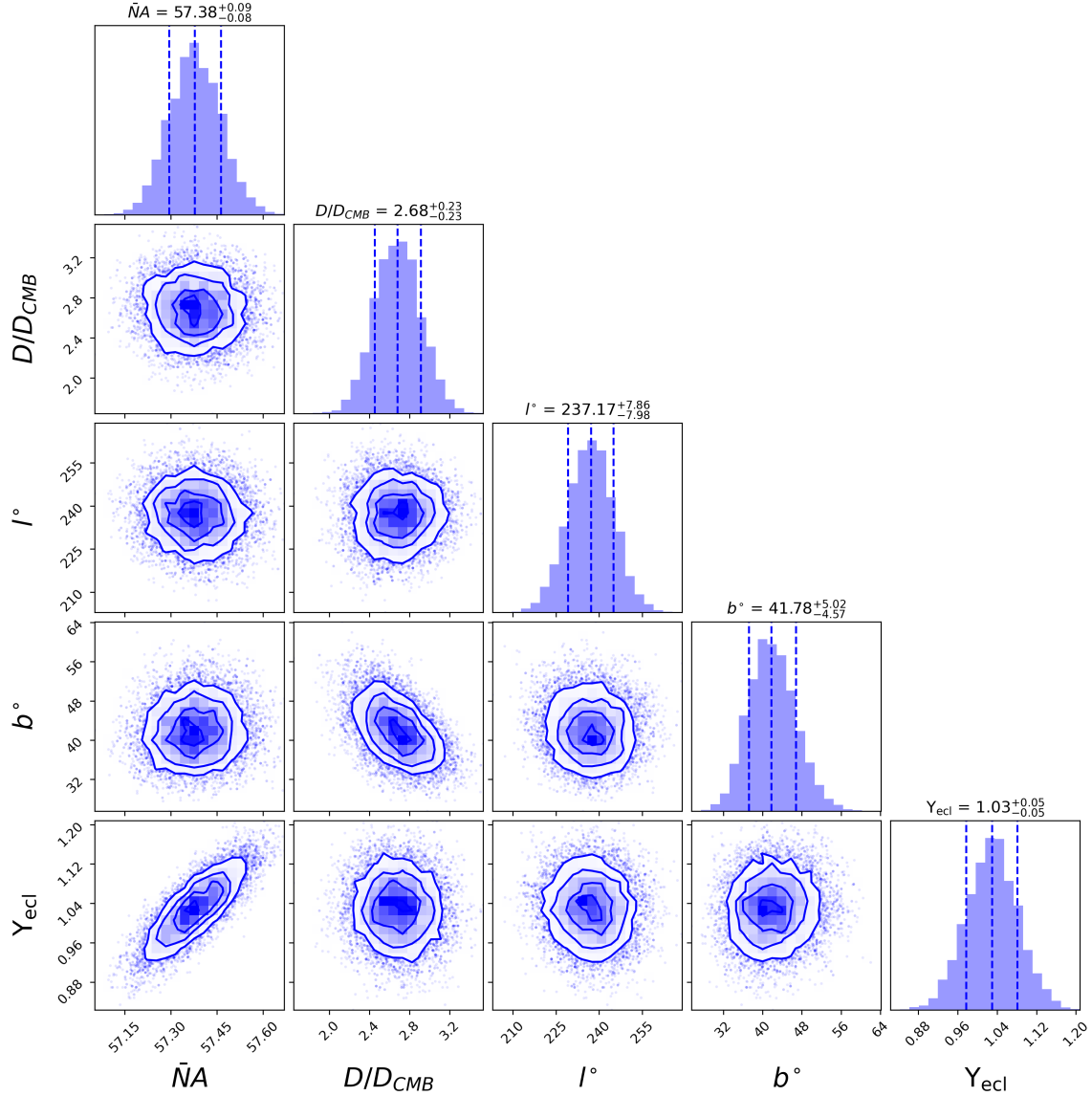


Figure 2. Corner plot for the results of the MCMC exploration of the posterior distribution. Dashed vertical lines indicate the mean and 68% confidence limits (as quoted). Here $\bar{N}A \equiv \bar{N}\Omega_{\text{pix}}$ is the mean number count per pixel, D/D_{CMB} is the dipole amplitude normalised relative to the CMB expectation, and Y_{ecl} is the ecliptic bias parameter; the Galactic coordinates (l, b) specify the direction of the dipole \mathbf{d} on the sky. Note that $D_{\text{CMB}} = 0.0072$, as determined from the CMB velocity (1) and the sample’s mean values $\bar{\alpha} = 1.26$ and $\bar{\chi} = 1.7$. The contours correspond to 0.5, 1, 1.5, and 2σ , encompassing 11.8%, 39.3%, 67.5%, and 86.4% of the samples, respectively (Foreman-Mackey 2016).

the scaled amplitude of the dipole, D/D_{CMB} , between 0 and 10; as noted in S21, the expected amplitude of dipole is $D_{\text{CMB}} = 0.0072$ (for the sample’s mean values $\bar{\alpha} = 1.26$ and $\bar{\chi} = 1.7$). The direction of the dipole in l and b were chosen to give a uniform distribution over the entire sphere, for $0^\circ < l < 360^\circ$ and $-90^\circ < b < 90^\circ$. A uniform prior was adopted for the ecliptic bias, $-2 < Y_{\text{ecl}} < 2$.

The resulting Bayesian evidences for the various hypotheses are presented in Table 1. There are two immediate points to take from these. First, the null hypothesis of there being no dipole is overwhelmingly disfavoured, demonstrating that a non-homogeneous signature is present in the distribution of quasars. Second, the models correcting for the ecliptic bias are strongly favoured over those models that do not consider this component. Hence, in the following we will focus upon models M_6 , M_7 and M_8 .

It is clear that M_6 – which assumes a dipole with a fixed am-

plitude and direction to match the expectations of the kinematic dipole – is highly disfavoured when compared to M_7 and M_8 . For M_7 , where the amplitude of the dipole is free to vary, we find $D/D_{\text{CMB}} = 2.46 \pm 0.18$, demonstrating that, as with S21, the amplitude of the quasar dipole is significantly different to the expectation from the CMB. Intriguingly, the ratio of the Bayesian evidences for M_7 and M_8 is only 3, in favour of M_8 . Therefore, we find only mild evidence that the dipole direction differs from the CMB direction. For completeness, Fig. 2 presents the corner plot of the posterior distributions for M_8 . As well as showing the evidence for the ecliptic biasing as identified by S21, with $Y_{\text{ecl}} = 1.03 \pm 0.05$, again a significantly larger dipole amplitude, with $D/D_{\text{CMB}} = 2.68 \pm 0.23$, is identified. From the posterior distribution we compute $P(D > D_{\text{CMB}} | \mathcal{D}) = \int_{D_{\text{CMB}}}^{\infty} dD p(D | \mathcal{D})$, the probability that the CatWISE dipole amplitude exceeds the CMB value, all other parameters marginalised over.

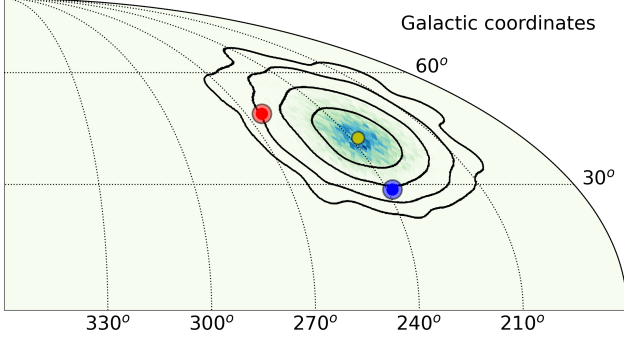


Figure 3. The on-sky posterior distribution of the direction of the dipole from the MCMC exploration, with the colour-coding corresponding to a distribution normalised to unity. The contours are derived from smoothing the underlying distribution with a Gaussian kernel with smoothing scale $\sigma = 3^\circ$, with each contour encompassing 68%, 95.5%, 99.7% and 99.99% of the probability. The yellow-filled circle indicates the point of the best-fit values, whereas the red-filled circle denotes the direction of the dipole as determined by Planck Collaboration et al. (2020a). The blue-filled circle represents the dipole direction as determined by S21.

We find $P(D > D_{\text{CMB}} | \mathcal{D}) = 0.999999888$, corresponding to a statistical significance of 5.7σ .

As for the direction of the dipole we find $(l, b) = (237.2^{+7.9}_{-8.0}, 41.8 \pm 5.0)$. The posterior distribution of the dipole directions on the sky is presented in Fig. 3, with contours indicating the 68%, 95.5%, 99.7% and 99.99% credible regions. The yellow-filled circle indicates the point of the best-fit values, whereas the red-filled circle denotes the direction of the dipole as determined by Planck Collaboration et al. (2020a). The blue-filled circle represents the dipole direction as determined by S21. As demonstrated by the ratio of the Bayesian evidences for M_7 and M_8 , this direction is only mildly favoured over the quasar dipole being aligned with that detected in the CMB.

It is important to note that Bayesian model selection calculations, such as those presented in this paper, can be affected by the choice of priors. Particularly, if we had used a narrower prior for the direction of the quasar dipole (i.e. if we had expected it to be *close* to the CMB direction), we would have found stronger evidence for a direction difference. On the other hand, if we had used a wider prior for parameters like $\bar{N}A$ that have the same meaning across models, this would decrease the evidence values across the board, but leave conclusions about the dipole unchanged. However, given that we should not necessarily expect *a priori* the quasar and CMB dipole to be aligned, we are justified in using the large prior range adopted.

3 A PRIORI PREDICTIONS FOR THE DIPOLE AMPLITUDE

In light of renewed interest in dipole anomalies it is worth revisiting the predictions of Λ CDM (e.g. Gibelyou & Huterer 2012; Rubart et al. 2014; Tiwari & Nusser 2016; Bengaly et al. 2019), without invoking the stringent CMB prior (1), which assumes a purely kinematic origin of the dipole. Here we are primarily interested in the distribution of values of the amplitude. In order to obtain this we will need the probability distribution of the dipoles themselves. The key assumption we will make is that the kinematic and clustering

dipoles are Gaussian distributed. This is justified in the case of the clustering dipole given that it is to a large degree sourced by matter fluctuations well described by linear theory. The kinematic dipole, on the other hand, is harder to justify. The local velocity is the result of several contributions, including the motion of the Earth around the Sun; the Sun around the Milky Way; the virial motion of the Milky Way within the Local Group, etc. Assigning a distribution to each of these motions is beyond what we can hope to achieve in this comparison. Here we will take a decidedly less fine-grained approach. We will assume that the local velocity admits a decomposition into a linear and nonlinear component, as described by the halo model. The linear contribution, due to infall onto large-scale structure, can then be described by linear theory and is Gaussian in nature. The nonlinear contribution is generically ascribed to virial motions within a spherical halo described as an isothermal sphere. In this case the motions are Gaussian for a given halo mass, in reasonable agreement with simulations (Sheth & Diaferio 2001). However, it is important to note that the probability distribution, averaged over all halo masses, is *not* Gaussian, exhibiting larger-than-Gaussian tail probabilities due to virial motions (Cooray & Sheth 2002). We will return to this point later in Section 3.4.

Now since the dipoles are Gaussian, the amplitude is described by the Maxwellian. This is in general a long-tailed distribution with large values of D not precluded. However, this is strictly only true for full-sky coverage; for partial-sky coverage the distribution is no longer Maxwellian due to the loss of isotropy. As we will show, in the partial-sky case there are non-trivial covariances between different multipole moments (e.g. in the clustering statistics), leading generically to a leakage of power from higher multipoles (smaller angular scales) into the dipole, changing the theoretical expectations of the amplitude. With 50% of the sky removed, the impact of masking is sizeable. In this section we will thus compare the posterior $p(D | \mathcal{D})$ obtained in the previous section, with the theoretical prior $p(D)$, the probability distribution of the total dipole amplitude $D = |\mathbf{d}|$ according to Λ CDM. Since the computation of $p(D)$ is somewhat involved we present here only the main results, relegating the technical details to appendices.

3.1 Dipole statistics

The dipole anisotropy has a direction and amplitude and it is convenient to represent it as a three-dimensional Cartesian vector \mathbf{d} such that $\mathbf{d} \cdot \hat{\mathbf{n}} = \sum_{m=-1}^1 a_{1m} Y_{1m}(\hat{\mathbf{n}})$, where $Y_{1m}(\hat{\mathbf{n}})$ are the $\ell = 1$ spherical harmonics (Copi, Huterer & Starkman 2004). Since the dipole is estimated on the masked sky, in order to compare with theoretical predictions we will need to take this into account. We will therefore write the number-count fluctuations as

$$\Delta N(\hat{\mathbf{n}})/N = \mathcal{W}(\hat{\mathbf{n}})(\mathbf{d}_k \cdot \hat{\mathbf{n}} + \delta_Q(\hat{\mathbf{n}})) = \mathcal{W}(\hat{\mathbf{n}})(\mathbf{d} \cdot \hat{\mathbf{n}} + \dots), \quad (10)$$

where $\mathcal{W}(\hat{\mathbf{n}})$ is the mask and $\mathbf{d} = \mathbf{d}_k + \mathbf{d}_c$. Here the ellipsis represent higher multipoles ($\ell \geq 2$) of the intrinsic fluctuations $\delta_Q(\hat{\mathbf{n}}) = \sum_{\ell m} a_{\ell m} Y_{\ell m}(\hat{\mathbf{n}})$. For Λ CDM these multipoles are subdominant to the dipole and may therefore be ignored. The underlying kinematic and clustering dipoles (on the unmasked sky) are uniquely given in terms of their harmonic coefficients by

$$\mathbf{d}_c = \sqrt{\frac{3}{4\pi}} (-\sqrt{2}\Re(a_{11}), \sqrt{2}\Im(a_{11}), a_{10})^\top, \quad (11a)$$

$$\mathbf{d}_k = \sqrt{\frac{3}{4\pi}} (-\sqrt{2}\Re(b_{11}), \sqrt{2}\Im(b_{11}), b_{10})^\top, \quad (11b)$$

with

$$a_{\ell m} = \int d^2 \hat{\mathbf{n}} Y_{\ell m}^*(\hat{\mathbf{n}}) \delta_Q(\hat{\mathbf{n}}), \quad (12a)$$

$$b_{\ell m} = \int d^2 \hat{\mathbf{n}} Y_{\ell m}^*(\hat{\mathbf{n}}) (\mathbf{d}_k \cdot \hat{\mathbf{n}}). \quad (12b)$$

Note that since $\mathbf{d}_k \cdot \hat{\mathbf{n}}$ is a pure dipole we have that only for $\ell = 1$ are the $b_{\ell m}$ non-zero. This is not the case for δ_Q , however.

In general, the fluctuation $\delta_Q(\hat{\mathbf{n}})$ results from a number of effects, including redshift-space distortions (Kaiser 1987), Doppler effects, gravitational lensing (Turner et al. 1984; Murray 2022), gravitational redshift, and relativistic corrections (Yoo, Fitzpatrick & Zaldarriaga 2009; Bonvin & Durrer 2011; Challinor & Lewis 2011). The complete expression for $\delta_Q(\hat{\mathbf{n}})$ can be found in, e.g. Di Dio et al. (2013, appendix A); we compute it using a modified version of CLASS (Blas, Lesgourgues & Tram 2011). Since the distribution of the amplitude is largely insensitive to the bias, here we simply fix the bias at the mean redshift using the Croom et al. (2005) quasar bias parametrisation. Here since $\bar{z} = 1.2$ we have $b_Q = 2$.

As for the individual statistics of \mathbf{d}_k and \mathbf{d}_c these are given by trivariate Gaussians. The joint distribution is also a Gaussian, containing non-trivial correlations between \mathbf{d}_k and \mathbf{d}_c . This is because the kinematic dipole is in part sourced from our being pulled by the surrounding matter distribution, implying that there is necessarily a clustering contribution. Since these two contributions arise from the same large-scale structure, and are linearly related to the matter distribution $\delta(\mathbf{x})$, their joint statistics must also be Gaussian. We will therefore take $(\mathbf{d}_k, \mathbf{d}_c) \sim \mathcal{N}(\mathbf{0}, \mathbf{C})$, with the 6×6 covariance matrix

$$\mathbf{C} = \begin{pmatrix} \langle \mathbf{d}_k \mathbf{d}_k^T \rangle & \langle \mathbf{d}_k \mathbf{d}_c^T \rangle \\ \langle \mathbf{d}_c \mathbf{d}_k^T \rangle & \langle \mathbf{d}_c \mathbf{d}_c^T \rangle \end{pmatrix}. \quad (13)$$

The structure of this covariance will depend on whether we are working on the full sky or the cut sky. For full-sky coverage each block matrix is proportional to the identity matrix (on account of isotropy), but in general it is more complex.

Note on account of equation (11) that the harmonic coefficients are linearly related to the dipole vectors, so are also Gaussian distributed. We will switch to the harmonic description (e.g. in Appendix D), which is more convenient when incorporating a masked.

3.2 Probability distribution of the amplitude

We are of course interested in the amplitude of the dipole, $D = |\mathbf{d}_k + \mathbf{d}_c|$, and in particular its distribution $p(D)$, the theoretical Λ CDM prior. It can be computed as follows. Since the amplitude depends on the individual dipoles, $D \equiv |\mathbf{d}_k + \mathbf{d}_c|$, we have by the chain rule

$$p(D) = \int d^3 \mathbf{d}_k \int d^3 \mathbf{d}_c p(D | \mathbf{d}_k, \mathbf{d}_c) p(\mathbf{d}_k, \mathbf{d}_c), \quad (14)$$

i.e. we marginalise over each dipole. Here $p(\mathbf{d}_k, \mathbf{d}_k) = \mathcal{N}(\mathbf{0}, \mathbf{C})$, whereas the relation between the amplitude and the dipoles is fixed, so $p(D | \mathbf{d}_k, \mathbf{d}_c) = \delta_D(D - |\mathbf{d}_k + \mathbf{d}_c|)$.

In the case of full-sky coverage the statistics of the dipoles are isotropic, and the marginalisation (14) yields the Maxwell–Boltzmann distribution, as is well known. In the more realistic case of partial-sky coverage the PDF is no longer Maxwellian; in general, the variances of each component are not identical. However, with the Galactic plane cut of S21 the marginalisation can still be done. We find (see Appendix C for details)

$$p(D) dD = (1 - \varepsilon) \mathcal{F}\left(\sqrt{|\varepsilon|} \frac{D}{\sqrt{2}\Delta_x}\right) f_{\text{MB}}\left(\frac{D}{\sqrt{2}\Delta_x}\right) \frac{dD}{\sqrt{2}\Delta_x}, \quad (15)$$

where $\mathcal{F}(x) \equiv F(x)/x$, in which $F(x) \equiv e^{-x^2} \int_0^x dt e^{t^2}$ is the Dawson function; we have introduced $\varepsilon \equiv 1 - \Delta_z^2/\Delta_x^2$, which parametrises the ‘eccentricity’ between the dispersions along the z -axis and the x -axis (or, equivalently, the y -axis) as induced by our azimuthal sky cut; and $f_{\text{MB}}(x)$ has the Maxwell–Boltzmann form, $f_{\text{MB}}(x) dx = 4/\sqrt{\pi} x^2 e^{-x^2} dx$. Here we have

$$\Delta_x^2 = \sigma_{k_x k_x}^2 + 2\sigma_{k_x c_x}^2 + \sigma_{c_x c_x}^2, \quad (16a)$$

$$\Delta_z^2 = \sigma_{k_z k_z}^2 + 2\sigma_{k_z c_z}^2 + \sigma_{c_z c_z}^2, \quad (16b)$$

which give the dispersions for the x - and z -components of the total dipole $\mathbf{d} = \mathbf{d}_k + \mathbf{d}_c$ (with the dispersion of the y -component the same as that of the x -component).¹ Notice that this PDF (15) is similar to the Maxwellian, save for the first two factors, which depend on the asymmetry of the cut. The overall effect of these factors suppresses the tail of the Maxwellian. The modified PDF has mean $\langle D \rangle = \sqrt{2/\pi} [\Delta_z + \Delta_x \text{arcsinh}(\sqrt{|\varepsilon|})/\sqrt{|\varepsilon|}]$, and r.m.s. value $\sqrt{\langle D^2 \rangle} = (3 - \varepsilon)^{1/2} \Delta_x$.² We find that the mean value $\langle D \rangle$ on the cut sky is half that on the full sky.

3.2.1 Λ CDM considerations

We now evaluate the probability distribution (15), plugging in the detailed predictions of Λ CDM for Δ_x^2 and Δ_z^2 . In general, for two tracers of large-scale structure, labelled X and Y , these dispersions are given in terms of the angular power spectra by

$$C_\ell^{XY} = 4\pi \int_0^\infty \frac{dk}{k} \Delta_\ell^X(k) \Delta_\ell^Y(k) \mathcal{P}(k), \quad (17)$$

where $\Delta_\ell^X(k)$ is the harmonic transfer function of X , and $\mathcal{P}(k)$ is the (dimensionless) power spectrum of primordial curvature perturbations $\zeta(\mathbf{k})$ defined by $\langle \zeta(\mathbf{k}) \zeta^*(\mathbf{k}') \rangle = (2\pi)^3 \delta_D(\mathbf{k} - \mathbf{k}') 2\pi^2 \mathcal{P}(k)/k^3$. The analytic forms of the kinematic ($X = k$) and clustering ($Y = c$) transfer functions are presented in Appendix A. Note that the clustering transfer function depends on the sample’s redshift distribution $p_z(z)$; this has been estimated by S21 by cross-matching a subsample of their sources with those in a subregion of SDSS (Stripe 82).

Since $\mathbf{d}_k = A_k \boldsymbol{\beta}$, where $\boldsymbol{\beta} = \mathbf{v}_O/c$ and $A_k \equiv 2 + x(1 + \alpha)$, to fix the statistics of the kinematic dipole we will need a model of the local velocity. We will take this velocity to be composed of a smooth part \mathbf{v}_R and a stochastic part \mathbf{v}_{vir} , i.e. $\mathbf{v}_O = \mathbf{v}_R + \mathbf{v}_{\text{vir}}$. The smooth part, coherent over large scales, can be described using linear perturbation theory; on the other hand the stochastic part, due to the virial motions of clusters, is nonlinear in nature. Given that \mathbf{v}_R and \mathbf{v}_{vir} arise from different physical processes, on different length scales, we will take these two types of motion to be uncorrelated, $\langle \mathbf{v}_R \mathbf{v}_{\text{vir}}^T \rangle = \langle \mathbf{v}_R \rangle \langle \mathbf{v}_{\text{vir}} \rangle^T = 0$.

The coherent part \mathbf{v}_R is sourced by the matter distribution, smoothed by a spherically-symmetric window function with char-

¹ Although \mathbf{d}_c here is not strictly a velocity, it is related to the underlying density field $\delta(\mathbf{x})$ (see Appendix A) so we will also consider it a ‘velocity’, with some associated dispersion.

² In the case of full-sky coverage we recover the Maxwellian, which has identical dispersion along each axis, $\Delta_x^2 = \Delta_y^2 = \Delta_z^2 \equiv \Delta^2$, with $\Delta^2 = \sigma_{kk}^2 + 2\rho\sigma_{kk}\sigma_{cc} + \sigma_{cc}^2$. We then have for the r.m.s. amplitude $\sqrt{\langle D^2 \rangle} = \sqrt{3}\Delta$, and mean $\langle D \rangle = \sqrt{8/\pi}\Delta \approx 0.92\sqrt{\langle D^2 \rangle}$.

Table 2. Cluster masses considered and the corresponding smoothing scales. Here σ_{vir} , σ_R , and $\sigma_{\text{tot}} = (\sigma_{\text{vir}}^2 + \sigma_R^2)^{1/2}$ are the one-dimensional dispersions.

M [$h^{-1} M_{\odot}$]	R [$h^{-1} \text{Mpc}$]	σ_{vir} [km s^{-1}]	σ_R [km s^{-1}]	σ_{tot} [km s^{-1}]
10^{12}	1.26	49	306	310
10^{13}	2.71	105	304	321
10^{14}	5.85	226	295	372
10^{15}	12.6	488	276	561

acteristic length R , i.e.

$$\begin{aligned} \mathbf{v}_R(\mathbf{x}) &\equiv \int d^3\mathbf{x}' W_R(\mathbf{x} - \mathbf{x}') \mathbf{v}(\mathbf{x}') \\ &= \int \frac{d^3\mathbf{k}}{(2\pi)^3} \frac{-i\mathbf{k}}{k} \left(\frac{H_0 f_0}{k} \right) W(kR) \delta(\mathbf{k}) e^{-i\mathbf{k}\cdot\mathbf{x}}. \end{aligned} \quad (18)$$

Here $f_0 \approx \Omega_{m0}^{0.55}$ is the present-day growth rate, and in the second line we have used the linearised continuity equation to relate the velocity to the matter distribution. In this work we adopt a spherical top-hat filter for which $W(kR) = 3j_1(kR)/(kR)$, where R is the comoving Lagrangian radius associated with mass M through $M = 4\pi R^3 \bar{\rho}_{m0}/3$.

The virial motion is assumed to be that of an isothermal sphere of mass M (Sheth & Diaferio 2001). Then, by the virial theorem, $\sigma_{\text{vir}}^2 \propto M/R_{\text{vir}} \propto M^{2/3}$, and by isotropy $\langle \mathbf{v}_{\text{vir}} \mathbf{v}_{\text{vir}}^T \rangle = \sigma_{\text{vir}}^2 \mathbf{I}_3$. We will compute the present-time velocity dispersion using the fitting formula (Bryan & Norman 1998)

$$\sigma_{\text{vir}}(M) = \frac{1}{\sqrt{3}} 476 g_{\sigma} \Delta_{\text{vir}}^{1/6} \left(\frac{M}{10^{15} h^{-1} M_{\odot}} \right)^{1/3} \text{km s}^{-1}, \quad (19)$$

where $g_{\sigma} = 0.9$, and $\Delta_{\text{vir}} = 18\pi^2 + 60y - 32y^2$, with $y = \Omega_{m0} - 1$.

In summary, the dispersions $\sigma_{k_x k_x}^2$, $\sigma_{k_x c_x}^2$, $\sigma_{c_x c_x}^2$, etc, are given in terms of linear combinations of the full-sky dispersions σ_{kk}^2 , σ_{kc}^2 , and σ_{cc}^2 , (see Appendix D3 for full expressions), which in terms of the angular power read

$$\sigma_{kk}^2 = \frac{3}{4\pi} C_1^{\text{kk}} + A_k^2 (\sigma_{\text{vir}}/c)^2, \quad (20a)$$

$$\sigma_{cc}^2 = \frac{3}{4\pi} (C_1^{\text{cc}} + 1/\bar{N}), \quad (20b)$$

$$\sigma_{kc}^2 = \frac{3}{4\pi} C_1^{\text{kc}}, \quad (20c)$$

where C_1^{kk} , C_1^{cc} , and C_1^{kc} are evaluated using equation (17) and the appropriate transfer functions. For the clustering dispersion we have also taken into account that number counts are Poisson distributed, thus generating in σ_{cc}^2 a shot-noise contribution $C_1^{\text{shot}} = 1/\bar{N}$, where $\bar{N} = N_{\text{tot}}/(4\pi f_{\text{sky}})$ is the mean number-count density. In this work $N_{\text{tot}} = 1,355,352$ and here $f_{\text{sky}} = 0.5$, giving $\bar{N} = 215,711$ (about 69 sources per square degree). Note that with the kinematic transfer function (A10) the kinematic dispersion may also be written as $\sigma_{kk}^2 = A_k^2 (\sigma_R^2 + \sigma_{\text{vir}}^2)/c^2$, with the usual (one-dimensional) velocity dispersion

$$\sigma_R^2 = \frac{1}{3} \int_0^{\infty} \frac{k^2 dk}{2\pi^2} \left(\frac{H_0 f_0}{k} \right)^2 W^2(kR) P(k), \quad (21)$$

where $P(k)$ is the matter power spectrum. The velocity dispersions considered in this work are given in Table 2. For each velocity dispersion we show in Fig. 4 the corresponding PDF presented earlier [equation (15)]. Note that in all PDFs the dispersions corresponding to shot noise and clustering are fixed to the same values (they are

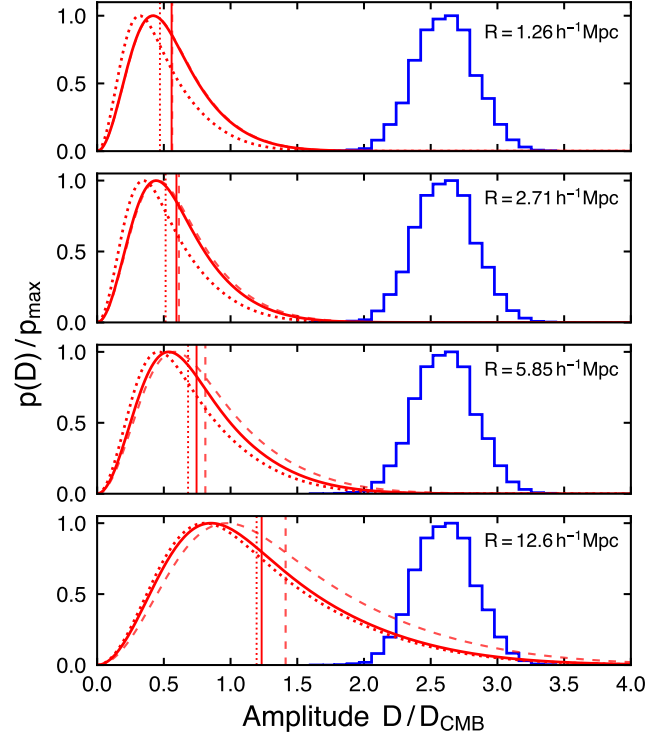


Figure 4. Comparison between the theoretical prior (red) and the recovered posterior (blue; as shown in Fig. 2) of the dipole amplitude. (Note that the posterior is based on a uniform prior on D .) In each subplot – corresponding to a different smoothing length, or velocity dispersion – we show the theoretical prior with contributions from clustering (solid curve) and without them (dotted curve); the dashed curve indicates the distribution when both clustering and the maximal source-evolution correction are included ($\rho = 1$; see equation (25)). The vertical lines indicate the means of the respective probability densities. Here we have taken $x = 1.7$ (corresponding to a magnification bias of $s = 2x/5 = 0.68$), and adopted the *Planck* 2018 best-fit spatially-flat Λ CDM cosmology (Planck Collaboration et al. 2020b).

independent of R). However, the covariance between clustering and kinematics (e.g. $\sigma_{k_x c_x}^2$) varies depending on R , as with the purely kinematic dispersion.

Clearly our results will depend on the rather subjective value of R (or M). Continuing our probabilistic approach, one way around this is to simply marginalise over this uncertainty. In order to do this we need to assign a prior $p(M)$, the distribution of masses. This is given by the halo mass function dn/dM , for which we use the mass function of Sheth & Tormen (1999). Thus the distribution of amplitudes, marginalised over all masses between some interval, is

$$p(D) = \int dM p(D | M) p(M) = \int dM p(D | M) \frac{M}{\rho_m} \frac{dn}{dM}, \quad (22)$$

where $p(D | M)$ is the probability distribution given by equation (14) and $\rho_m = \int dM M dn/dM$ (all matter in halos). This distribution is shown in Fig. 5. Compared with equation (15), this distribution exhibits a slightly heavier tail; this is also reflected in the difference between the mean and mode (cf. Fig. 4).

3.3 Effect of source evolution on \mathbf{d}_k

The kinematic dipole as given by equation (3) is idealised given that the source population likely evolves over time (Dalang & Bonvin 2022). Recall that this equation is based on a uniform sample of radio

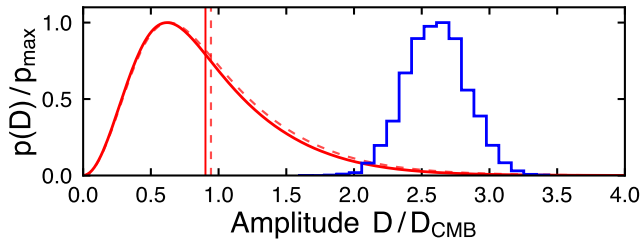


Figure 5. Comparison between the posterior and the marginalised theoretical prior (22). Here we use $M_{\min} = 10^{12}h^{-1}M_{\odot}$ and $M_{\max} = 10^{15}h^{-1}M_{\odot}$, and we include all contributions from clustering (which again have negligible impact).

sources, each with identical spectral index α , producing an integral source count with constant slope x at the flux density limit (Ellis & Baldwin 1984). In practice, there will be some amount of population variance among the measured α (as found by S21 in their CatWISE sample). Although this may be due to some intrinsic variation in AGN emission, it is also possible that it is in part due to α having some dependence on redshift. Moreover, in a flux-limited survey, the magnification bias $s = 2x/5$ generally depends on redshift: for a fixed flux threshold, the number of unobserved sources grows as the luminosity threshold is increased (i.e. the slope x is an increasing function of redshift).

Revisiting the derivation of equation (3) in a more general context, Dalang & Bonvin (2022) showed that when allowing $x = x(z)$ and $\alpha = \alpha(z)$ the kinematic dipole becomes

$$\mathbf{d}_k = \bar{A}_k \boldsymbol{\beta}, \quad \text{with} \quad \bar{A}_k \equiv \int dz p_z(z) [2 + x(z)(1 + \alpha(z))], \quad (23)$$

i.e. the prefactor in the standard formula (3) is replaced by its average over the source redshift distribution.³ (Note that the velocity $\boldsymbol{\beta}$ is still given at the observer’s position.) This integrated dipole generalises the standard form, which is recovered when either x or α are redshift independent, or one observes at fixed redshift.

Evaluating the integrated dipole requires knowledge of $x(z)$, which we here do not have without a measurement of the quasar luminosity function (Wang et al. 2020; Guandalin et al. 2022). Since \bar{A}_k is given as the expectation over the sample we will instead consider an equivalent but more suggestive form:

$$\bar{A}_k = \int dx \int d\alpha p(x, \alpha) [2 + x(1 + \alpha)], \quad (24)$$

where $p(x, \alpha)$ is the joint distribution, for which we have from S21 an empirical estimate of its marginal $p(\alpha)$ (based on measurements of α from W1 and W2 bands). From this equation we have that [cf. equation (3)]

$$\bar{A}_k = [2 + \bar{x}(1 + \bar{\alpha})] + \rho \sigma_x \sigma_\alpha = A_k + \rho \sigma_x \sigma_\alpha, \quad (25)$$

where $\bar{x} = \int dx x p(x)$ and $\bar{\alpha} = \int d\alpha \alpha p(\alpha)$ denote the means; $\sigma_x = \langle (x - \bar{x})^2 \rangle^{1/2}$ and $\sigma_\alpha = \langle (\alpha - \bar{\alpha})^2 \rangle^{1/2}$ the variances; and $\rho \equiv \langle (x - \bar{x})(\alpha - \bar{\alpha}) \rangle / (\sigma_x \sigma_\alpha)$ the correlation coefficient between x and α . Thus we have a correction to the standard formula if $\langle x\alpha \rangle \neq \langle x \rangle \langle \alpha \rangle$,

³ Here we integrate along redshift instead of comoving distance, as done in Dalang & Bonvin (2022); both expressions of \mathbf{d}_k , however, are equivalent at linear order. Alternatively, instead of $\alpha(z)$, the integrated dipole can be expressed in terms of the evolution bias $f_{\text{evo}}(z)$, which parametrises how a tracer’s population number evolves over time (Maartens et al. 2018; Nadolny et al. 2021; Dalang & Bonvin 2022).

i.e. if $\rho \neq 0$. Although we do not have $x(z)$ nor $p(x)$, we do know its mean, $\bar{x} = 1.7$, as obtained from the whole sample. Based on this information alone we can nevertheless make progress. Continuing our Bayesian approach, we shall fix $p(x)$ according to the *principle of maximum entropy* (Jaynes 2003), that is, we choose for $p(x)$ that which maximises the information entropy $\int dx p(x) \ln p(x)$, subject to the constraint of known mean \bar{x} and the physical requirement that $x \geq 0$. This leads us to $p(x) = \lambda e^{-\lambda x}$, with $\lambda = 1/\bar{x}$, i.e. the exponential distribution. The mean is of course \bar{x} , and the variance $\sigma_x^2 = \bar{x}^2$. Separately, using the empirical distribution of α obtained by S21, we determine $\bar{\alpha} = 1.26$ and $\sigma_\alpha = 0.597$.

We can now estimate \bar{A}_k using equation (25). Though this requires the unknown correlation coefficient ρ , we do however have an upper limit on it. Thus with $\rho = 1$ we have a maximum correction of $\rho \sigma_x \sigma_\alpha \leq 1.7 \times 0.597 = 1.0$. It should be noted that this is not a strict upper limit for it depends on what one assigns to the rather uncertain $p(x)$. With this caveat in mind, we estimate $\bar{A}_k \leq 6.7$, that is, we have a correction to the standard prefactor ($A_k = 5.8$) of no more than 17%. The distribution corresponding to this upper limit is shown in Fig. 4 (see dashed curve), where we see that the improvement in the tension is modest at best. Clearly, in order to fully reconcile the observed dipole amplitude in this manner we would require a substantially larger correction. But even with full knowledge of both $x(z)$ and $\alpha(z)$, a correction of the needed size seems unlikely, as mentioned in Dalang & Bonvin (2022).

3.4 Assessing the tension

Fig. 4 gives a side-by-side comparison of the CatWISE posterior together with the theoretical probability distribution of D according to Λ CDM (evaluated using the empirical distributions of the redshifts and measured spectral indices). The first point to note is that the clustering signal is much weaker than the kinematic signal. In particular, the contribution from cross-correlations between the clustering and kinematic dipole is roughly an order of magnitude larger than the clustering signal (but still small compared to the kinematic signal). Furthermore, we have set $b_Q = 2$ using the Croom et al. (2005) quasar bias parametrisation for our mean redshift $\bar{z} = 1.2$, although we note that $p(D)$ is rather insensitive to the choice of b_Q and time dependence, the main contribution coming from the kinematic terms. Indeed, the fact that the clustering signal is small is not entirely surprising: the quasar sample is made up in large part of sources mostly at moderate to high redshifts, with the vast majority (99%) of sources at $z > 0.1$, so that a large clustering dipole from a local population of sources is not expected. Nevertheless, this confirms that, even with a more complete calculation of the impact of clustering on the dipole (including magnification bias among other effects), the kinematic contribution to the CatWISE dipole remains the dominant component.

A comparison with the predictions on the full sky (Appendix C1) shows that the masking of the Galactic plane causes a significant loss of dipole power, and thus a decrease in the expected dipole amplitude. This is evident if we compare $p(D)$ with the mask (Fig. 4) and without the mask (Fig. C1): the presence of the mask suppresses the tail probabilities, shifting the mean towards smaller values. While the mixing of modes does result in a leakage of power from high multipoles into the dipole, it is not nearly enough to compensate the reduction in power of the dipole itself. This is clear from the shift of the distribution to smaller D , which makes prominent a long tail by which rather large amplitudes can still be accommodated by Λ CDM.

To what extent is the Λ CDM prior compatible with the posterior found? One way to summarise the discrepancy seen in Fig. 4 is to

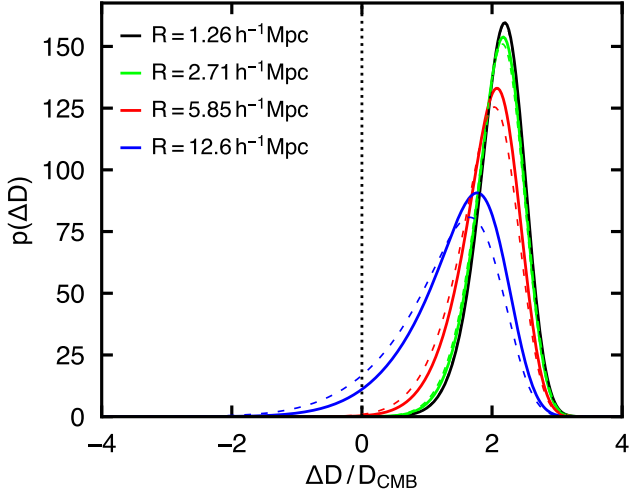


Figure 6. Normalised shift distribution (26) derived from the Λ CDM prior and posterior distributions for a range of smoothing lengths (as in Fig 4). Shown in dashed curves are the corresponding distributions with maximal source-evolution correction ($\rho = 1$).

compute the ‘tension statistic’ $T \equiv |\mu_1 - \mu_2|/(\sigma_1^2 + \sigma_2^2)^{1/2}$ for two distributions p_1 and p_2 , with means μ_1 and μ_2 , and variances σ_1^2 and σ_2^2 . But this is a rather crude measure when at least one of the distributions are non-Gaussian, as is the case for our prior (15). A more comprehensive way to quantify the discrepancy is to consider the PDF of the differences $\Delta D = D_1 - D_2$ (Raveri & Hu 2019):

$$p(\Delta D) = \int_{-\infty}^{\infty} dD p_1(D - \Delta D) p_2(D), \quad (26)$$

where $p_1(D_1)$ is the theoretical prior and $p_2(D_2)$ is the posterior. Note that because there is zero probability of finding a negative amplitude, this is essentially a one-sided convolution. (This integral is evaluated using a posterior smoothed by kernel density estimation.) The result is shown in Fig. 6. Unsurprisingly, we see that $p(\Delta D)$ has most support when ΔD is far from zero, peaking around $\Delta D \approx 2D_{\text{CMB}}$ (corresponding roughly to the difference of the means of the prior and posterior distribution). Thus the probability of finding any $\Delta D > 0$ is given by $P(\Delta D > 0) = \int_0^{\infty} d\Delta D p(\Delta D)$. From this probability we can compute a statistical significance using the ‘rule of thumb’ that the number of sigma be equal to $\sqrt{2} \text{erf}^{-1}(P(\Delta D > 0))$.⁴ Depending on the choice of R , we find tensions at the level of 5.8σ , 5.5σ , 4.3σ , and 2.1σ (from smallest to largest R). Note that these tensions are only marginally reduced when including the source-evolution corrections described in Section 3.3.

By contrast when we marginalise over all masses between our lower and upper limit, $M = 10^{12} h^{-1} M_{\odot}$ and $M = 10^{15} h^{-1} M_{\odot}$ (corresponding to $R = 1.26 h^{-1} \text{Mpc}$ and $R = 12.6 h^{-1} \text{Mpc}$), we find by equation (22) a tension of 3.8σ (and 3.6σ with source-evolution correction). This is still a considerable tension but less severe than suggested above. The slight easing of the tension is due to the fact that the tail probabilities of this distribution are larger than that of the corresponding distribution without marginalisation. This is evident in Fig. 5, which shows a small overlap of the tail with the posterior.

⁴ This reduces to the aforementioned T statistic in the case that $p(\Delta D)$ is Gaussian.

4 CONCLUSIONS

We have reanalysed the CatWISE quasar sample of Secrest et al. (2021b, S21) using a Bayesian approach. By comparison of several hypotheses, we found that the data was best described by a dipole with amplitude $D = (19 \pm 2) \times 10^{-3}$ and direction $(l, b) = (237^{\circ} 2_{-8^{\circ} 0}^{+7^{\circ} 9}, 41^{\circ} 8 \pm 5^{\circ} 0)$. Several parametric models were investigated. With the dipole amplitude free to vary, this dipole direction is only mildly preferred over a dipole aligned with the CMB, more so than that found by S21. However, it is important to note that the *amplitude* is considerably larger than expected from the conventional kinematic interpretation: accepting that the CMB dipole is produced entirely by our kinematic motion, our dipole converts to a speed of 1002 km s^{-1} relative to the CMB frame, a factor of 2.7 larger than the putative speed of 370 km s^{-1} . Taking into account the full posterior distribution (marginalising over all other parameters) we find a discrepancy at the 5.7σ level. While our inferred amplitude is somewhat larger than that found by S21 using a different estimation technique ($D = 15.54 \times 10^{-3}$), the qualitative conclusion of an anomalously large amplitude (with direction in good agreement with that of the CMB dipole) appears to be robust to methodological differences of analysis.

A comparison of the posterior with the theoretical prior indicates the extent of the discrepancy for Λ CDM. In order to perform this comparison we applied a mask to the underlying number-count fluctuations, imposing the same Galactic plane cut as in the analysis. The mask was found to have a considerable effect on the likely values of the dipole amplitude and its distribution. In particular, we found that the full-sky distribution overestimates the likely values of the amplitude, worsening the tension. Additionally, we have considered a redshift dependence in the spectral properties of the kinematic dipole, finding a slight easing of the tension – though we cannot claim with confidence that such an effect is small, given the limitations of our analysis relating to the unknown CatWISE distribution (or redshift dependence) of the magnification bias. But based on our present findings we conclude that the CatWISE dipole remains a puzzle for the standard model of cosmology.

NOTE ADDED

Since this manuscript was submitted, a work by Wagenfeld, Klöckner & Schwarz (2023) appeared in which the radio dipole is estimated from the Rapid ASKAP Continuum Survey (RACS) and the NRAO VLA Sky Survey (NVSS) catalogue data, extending the Bayesian method presented here to take into account systematics relevant to these catalogues. From a combined analysis of RACS and NVSS, they find a dipole with direction perfectly aligned with the CMB but with amplitude exceeding the expected value by a factor of about three at 4.8σ , in good agreement with the results reported here.

ACKNOWLEDGEMENTS

We thank Secrest et al. (2021b) for making public their data and analysis code, and the anonymous referee for a helpful report. LD thanks Camille Bonvin for useful discussions on the effect of source evolution. LD was supported by the Australian Government Research Training Program. A preliminary version of this work appeared in Dam (2021). GFL received no financial support for this research. This research made use of the Python packages NUMPY (Harris et al. 2020), MATPLOTLIB (Hunter 2007), HEALPIX (Górski et al. 2005; Zonca et al. 2019), CORNER (Foreman-Mackey 2016), and

GETDIST (Lewis 2019). Initial explorations of the posterior probability space were made using EMCEE (Foreman-Mackey et al. 2013) and DYNesty (Skilling 2004; Skilling 2006; Higson et al. 2019; Speagle 2020).

STATEMENT OF CONTRIBUTION

The statistical analysis of the CatWISE quasar sample, including the exploration of the posterior distributions and calculation of the Bayesian evidence was primarily undertaken by GFL and BJB, after preliminary analysis with LD. The calculation of the dipole's likely amplitude and the comparison with the posterior distributions was undertaken by LD. All authors contributed to the interpretation of the results and the writing of the paper.

DATA AVAILABILITY

The data and code used in this project will be made available upon reasonable request to the authors.

References

Aluri P. K., et al., 2023, *Class. Quant. Grav.*, 40, 094001
 Bengaly C. A. P., Maartens R., Santos M. G., 2018, *J. Cosmology Astropart. Phys.*, 2018, 031
 Bengaly C. A. P., Siewert T. M., Schwarz D. J., Maartens R., 2019, *MNRAS*, 486, 1350
 Blake C., Wall J., 2002, *Nature*, 416, 150
 Blas D., Lesgourgues J., Tram T., 2011, *J. Cosmology Astropart. Phys.*, 2011, 034
 Bonvin C., Durrer R., 2011, *Phys. Rev. D*, 84, 063505
 Brewer B. J., Foreman-Mackey D., 2018, *Journal of Statistical Software*, 86, 1–33
 Bryan G. L., Norman M. L., 1998, *ApJ*, 495, 80
 Challinor A., Lewis A., 2011, *Phys. Rev. D*, 84, 043516
 Colin J., Mohayaee R., Rameez M., Sarkar S., 2017, *MNRAS*, 471, 1045
 Condon J. J., Cotton W. D., Greisen E. W., Yin Q. F., Perley R. A., Taylor G. B., Broderick J. J., 1998, *AJ*, 115, 1693
 Cooray A., Sheth R. K., 2002, *Phys. Rept.*, 372, 1
 Copi C. J., Huterer D., Starkman G. D., 2004, *Phys. Rev. D*, 70, 043515
 Croom S. M., et al., 2005, *MNRAS*, 356, 415
 Dahlen F. A., Simons F. J., 2008, *Geophys. J. Int.*, 174, 774
 Dalang C., Bonvin C., 2022, *MNRAS*, 512, 3895
 Dam L., 2021, PhD thesis, <https://hdl.handle.net/2123/27817>
 Darling J., 2022, *Astrophys. J. Lett.*, 931, L14
 Di Dio E., Montanari F., Lesgourgues J., Durrer R., 2013, *J. Cosmology Astropart. Phys.*, 2013, 044
 Domènech G., Mohayaee R., Patil S. P., Sarkar S., 2022, *JCAP*, 10, 019
 Ellis G. F. R., Baldwin J. E., 1984, *MNRAS*, 206, 377
 Foreman-Mackey D., 2016, *The Journal of Open Source Software*, 1, 24
 Foreman-Mackey D., Hogg D. W., Lang D., Goodman J., 2013, *Publications of the Astronomical Society of the Pacific*, 125, 306–312
 Gibelyou C., Huterer D., 2012, *MNRAS*, 427, 1994
 Górski K. M., Hivon E., Banday A. J., Wandelt B. D., Hansen F. K., Reinecke M., Bartelmann M., 2005, *ApJ*, 622, 759
 Guandalin C., Piat J., Clarkson C., Maartens R., 2022, arXiv e-prints, p. [arXiv:2212.04925](https://arxiv.org/abs/2212.04925)
 Harris C. R., et al., 2020, *Nature*, 585, 357
 Higson E., Handley W., Hobson M., Lasenby A., 2019, *Statistics and Computing*, 29, 891
 Hivon E., Górski K. M., Netterfield C. B., Crill B. P., Prunet S., Hansen F., 2002, *ApJ*, 567, 2
 Hunter J. D., 2007, *Computing in Science & Engineering*, 9, 90

Jaynes E. T., 2003, *Probability Theory: The Logic of Science*. Cambridge University Press
 Kaiser N., 1987, *MNRAS*, 227, 1
 Lacy M., et al., 2020, *PASP*, 132, 035001
 Lewis A., 2019, arXiv e-prints, p. [arXiv:1910.13970](https://arxiv.org/abs/1910.13970)
 Maartens R., 2011, *Philosophical Transactions of the Royal Society of London Series A*, 369, 5115
 Maartens R., Clarkson C., Chen S., 2018, *J. Cosmology Astropart. Phys.*, 2018, 013
 Mainzer A., et al., 2014, *ApJ*, 792, 30
 Marocco F., et al., 2021, *ApJS*, 253, 8
 Mauch T., Murphy T., Buttery H. J., Curran J., Hunstead R. W., Piestrzynski B., Robertson J. G., Sadler E. M., 2003, *MNRAS*, 342, 1117
 McConnell D., et al., 2020, *Publ. Astron. Soc. Australia*, 37, e048
 Murray C., 2022, *MNRAS*, 510, 3098
 NIST DLMF 2023, NIST Digital Library of Mathematical Functions, <https://dlmf.nist.gov/>
 Nadolny T., Durrer R., Kunz M., Padmanabhan H., 2021, *J. Cosmology Astropart. Phys.*, 2021, 009
 Peebles P. J. E., 1980, *The Large-Scale Structure of the Universe*. Princeton University Press, Princeton, NJ
 Peebles P. J., Wilkinson D. T., 1968, *Physical Review*, 174, 2168
 Planck Collaboration et al., 2020a, *A&A*, 641, A3
 Planck Collaboration et al., 2020b, *A&A*, 641, A6
 Raveri M., Hu W., 2019, *Phys. Rev. D*, 99, 043506
 Rengelink R. B., Tang Y., de Bruyn A. G., Miley G. K., Bremer M. N., Roettgering H. J. A., Bremer M. A. R., 1997, *A&AS*, 124, 259
 Rubart M., Schwarz D. J., 2013, *A&A*, 555, A117
 Rubart M., Bacon D., Schwarz D. J., 2014, *A&A*, 565, A111
 Secrest N., von Hausegger S., Rameez M., Mohayaee R., Sarkar S., Colin J., 2021a, A Test of the Cosmological Principle with Quasars, [doi:10.5281/zenodo.4448512](https://doi.org/10.5281/zenodo.4448512), <https://doi.org/10.5281/zenodo.4448512>
 Secrest N. J., von Hausegger S., Rameez M., Mohayaee R., Sarkar S., Colin J., 2021b, *ApJ*, 908, L51
 Sheth R. K., Diaferio A., 2001, *MNRAS*, 322, 901
 Sheth R. K., Tormen G., 1999, *MNRAS*, 308, 119
 Siewert T. M., Schmidt-Rubart M., Schwarz D. J., 2021, *A&A*, 653, A9
 Singal A. K., 2011, *ApJ*, 742, L23
 Skilling J., 2004, in Fischer R., Preuss R., Toussaint U. V., eds, *American Institute of Physics Conference Series Vol. 735, Bayesian Inference and Maximum Entropy Methods in Science and Engineering*. pp 395–405
 Skilling J., 2006, *Bayesian Analysis*, 1, 833
 Speagle J. S., 2020, *MNRAS*, 493, 3132
 Stern D., et al., 2012, *ApJ*, 753, 30
 Stewart J. M., Sciamia D. W., 1967, *Nature*, 216, 748
 Tiwari P., Nusser A., 2016, *J. Cosmology Astropart. Phys.*, 2016, 062
 Turner M. S., 1991, *Phys. Rev. D*, 44, 3737
 Turner E. L., Ostriker J. P., Gott J. R. I., 1984, *ApJ*, 284, 1
 Wagnveld J. D., Klöckner H. R., Schwarz D. J., 2023, *A&A*, 675, A72
 Wang M. S., Beutler F., Bacon D., 2020, *MNRAS*, 499, 2598
 Wright E. L., et al., 2010, *AJ*, 140, 1868
 Yoo J., Fitzpatrick A. L., Zalzarriaga M., 2009, *Phys. Rev. D*, 80, 083514
 Zonca A., Singer L., Lenz D., Reinecke M., Rosset C., Hivon E., Gorski K., 2019, *Journal of Open Source Software*, 4, 1298

APPENDIX A: DETAILS ON THE THEORETICAL DIPOLE

Here we compute the kinematic and clustering dipoles in terms of the harmonic transfer functions, Δ_ℓ^k and Δ_ℓ^c , respectively. First, we recall that for a general field $O(\hat{\mathbf{n}})$ the coefficients $a_{\ell m}$ can always be expressed as a \mathbf{k} -space integral over the primordial perturbations, weighted by the appropriate harmonic transfer function $\Delta_\ell(k)$:

$$a_{\ell m} = (-i)^\ell 4\pi \int \frac{d^3\mathbf{k}}{(2\pi)^3} Y_{\ell m}^*(\hat{\mathbf{k}}) \Delta_\ell(k) \zeta(\mathbf{k}). \quad (\text{A1})$$

Then given the transfer functions for any two observables, labelled A and B , the spectrum C_ℓ^{AB} is given by

$$C_\ell^{AB} = 4\pi \int_0^\infty \frac{dk}{k} \Delta_\ell^A(k) \Delta_\ell^B(k) \mathcal{P}(k), \quad (\text{A2})$$

where we assume a standard primordial (adiabatic) power spectrum $\mathcal{P}(k)$ defined by $\langle \zeta(\mathbf{k}) \zeta^*(\mathbf{k}') \rangle = (2\pi)^3 \delta_{\mathbf{D}}(\mathbf{k} - \mathbf{k}') 2\pi^2 \mathcal{P}(k)/k^3$. In principle, superhorizon isocurvature fluctuations can also be considered, which are known to give rise to an intrinsic dipole in the CMB (Turner 1991). However, it was recently shown (Domènech et al. 2022) that such modes cannot also induce a sizeable intrinsic dipole in the number counts.

Now, using equations (A1) and (11), we find that the model prediction for the dipoles \mathbf{d}_X , $X \in \{k, c\}$, can be written as

$$\mathbf{d}_X = -4\pi i \sqrt{\frac{3}{4\pi}} \int \frac{d^3\mathbf{k}}{(2\pi)^3} \mathbf{U}^\dagger \mathbf{Y}_1(\hat{\mathbf{k}}) \Delta_1^X(k) \zeta(\mathbf{k}), \quad (\text{A3})$$

where $\mathbf{Y}_1 \equiv (Y_{1-1}, Y_{11}, Y_{10})^\top$ and we have the unitary matrix

$$\mathbf{U} = \begin{pmatrix} 1/\sqrt{2} & i/\sqrt{2} & 0 \\ -1/\sqrt{2} & i/\sqrt{2} & 0 \\ 0 & 0 & 1 \end{pmatrix}, \quad (\text{A4})$$

with $\mathbf{U}\mathbf{U}^\dagger = \mathbf{U}^\dagger\mathbf{U} = \mathbf{I}_3$. Note that $\mathbf{U}^\dagger \mathbf{Y}_1$ is a vector containing the $\ell = 1$ real-valued spherical harmonics.

Computing the statistics of \mathbf{d}_X – i.e. $\langle d_{X_i} d_{Y_j} \rangle = \sigma_{XY}^2 \delta_{ij}^K$ – is now straightforward. To obtain the dispersion σ_{XY}^2 we can simply select the z -component, all components being statistically equivalent under isotropy. Using orthogonality of spherical harmonics, we have

$$\sigma_{XY}^2 = 3 \int_0^\infty \frac{dk}{k} \Delta_1^X(k) \Delta_1^Y(k) \mathcal{P}(k) = \frac{3}{4\pi} C_1^{XY}, \quad (\text{A5})$$

where we have used $\langle \zeta(\mathbf{k}) \zeta^*(\mathbf{k}') \rangle = (2\pi)^3 \delta_{\mathbf{D}}(\mathbf{k} - \mathbf{k}') 2\pi^2 \mathcal{P}(k)/k^3$.

Note that in this appendix the $a_{\ell m}$'s belong to the full sky. Those belonging to the cut sky can always be obtained in terms of the full-sky $a_{\ell m}$'s by geometric linear relations. The explicit expressions are given later in Appendix D2.

A1 Clustering transfer function

Clustering gives rise to fluctuations $\delta_Q(\hat{\mathbf{n}})$ in the number counts. In spherical harmonics,

$$\delta_Q(\hat{\mathbf{n}}) = \sum_{\ell, m} a_{\ell m} Y_{\ell m}(\hat{\mathbf{n}}), \quad a_{\ell m} = \int d^2\hat{\mathbf{n}} Y_{\ell m}^*(\hat{\mathbf{n}}) \delta_Q(\hat{\mathbf{n}}). \quad (\text{A6})$$

Here we are interested in the dipole $\mathbf{d}_c \cdot \hat{\mathbf{n}} = \sum_{m=-1}^1 a_{1m} Y_{1m}(\hat{\mathbf{n}})$. Substituting $\delta_Q(\hat{\mathbf{n}}) = \int dz p_z(z) \delta_Q(\hat{\mathbf{n}}, z)$, with p_z the normalised redshift distribution, and the Fourier representation of $\delta_Q(\hat{\mathbf{n}}, z)$, we have

$$\begin{aligned} a_{\ell m} &= \int d^2\hat{\mathbf{n}} Y_{\ell m}^*(\hat{\mathbf{n}}) \int_0^\infty dz p_z(z) \delta_Q(\hat{\mathbf{n}}, z) \\ &= \int d^2\hat{\mathbf{n}} Y_{\ell m}^*(\hat{\mathbf{n}}) \int_0^\infty dz p_z(z) \int \frac{d^3\mathbf{k}}{(2\pi)^3} \delta_Q(\mathbf{k}, z) e^{-i\mathbf{k} \cdot \chi(z) \hat{\mathbf{n}}}, \end{aligned}$$

where in the second line we write $\mathbf{x} = \chi(z) \hat{\mathbf{n}}$. Now substituting the plane-wave expansion, $e^{-i\mathbf{k} \cdot \chi \hat{\mathbf{n}}} = \sum_{\ell, m} (-i)^\ell 4\pi j_\ell(k\chi) Y_{\ell m}^*(\hat{\mathbf{k}}) Y_{\ell m}(\hat{\mathbf{n}})$, into the foregoing expression

we find

$$\begin{aligned} a_{\ell m} &= \int d^2\hat{\mathbf{n}} Y_{\ell m}^*(\hat{\mathbf{n}}) \int_0^\infty dz p_z(z) \int \frac{d^3\mathbf{k}}{(2\pi)^3} \delta_Q(\mathbf{k}, z) \\ &\quad \times \sum_{\ell', m'} (-i)^{\ell'} 4\pi j_{\ell'}(k\chi(z)) Y_{\ell' m'}^*(\hat{\mathbf{k}}) Y_{\ell' m'}(\hat{\mathbf{n}}) \\ &= (-i)^\ell 4\pi \int \frac{d^3\mathbf{k}}{(2\pi)^3} Y_{\ell m}^*(\hat{\mathbf{k}}) \\ &\quad \times \left[\int_0^\infty dz p_z(z) b_Q(z) \mathcal{T}_\delta(k, z) j_\ell(k\chi(z)) + \dots \right] \zeta(\mathbf{k}), \end{aligned}$$

where in the second line we used the orthogonality of spherical harmonics. Here we have inserted $\delta_Q(\mathbf{k}, z) = b_Q(z) \delta(\mathbf{k}, z) + \dots = b_Q(z) \mathcal{T}_\delta(k, z) \zeta(\mathbf{k}) + \dots$, where the ellipsis are corrections from redshift-space distortions, Doppler effects, and general-relativistic corrections (see, e.g., Di Dio et al. 2013, appendix A, for complete expressions). We thus have

$$\Delta_\ell^c(k) = \int_0^\infty dz p_z(z) b_Q(z) \mathcal{T}_\delta(k, z) j_\ell(k\chi(z)) + \dots \quad (\text{A7})$$

A2 Kinematic transfer function

For the kinematic dipole recall that $\mathbf{d}_k \cdot \hat{\mathbf{n}} = A_k \boldsymbol{\beta} \cdot \hat{\mathbf{n}}$, with $A_k = 2 + x(1 + \alpha)$ and $\boldsymbol{\beta} = \mathbf{v}_O/c = \mathbf{v}(\mathbf{x}=0)/c$. In harmonics,

$$\mathbf{d}_k \cdot \hat{\mathbf{n}} = \sum_{L, M} b_{LM} Y_{LM}(\hat{\mathbf{n}}), \quad b_{LM} = \int d^2\hat{\mathbf{n}} Y_{LM}^*(\hat{\mathbf{n}}) \mathbf{d}_k \cdot \hat{\mathbf{n}}, \quad (\text{A8})$$

the calculation carries through in much the same way as with the previous calculation for number counts, provided that we keep \mathbf{x} arbitrary, setting $\mathbf{x} = 0$ only at the end of the calculation. (Note that since we are dealing with a pure dipole only $L = 1$ coefficients are nonzero.) We thus write equation (11b) as

$$\begin{aligned} b_{1M} &= \int d^2\hat{\mathbf{n}} Y_{1M}^*(\hat{\mathbf{n}}) A_k \mathbf{v}_R(\mathbf{x}=0) \cdot \hat{\mathbf{n}} / c \\ &= \int d^2\hat{\mathbf{n}} Y_{1M}^*(\hat{\mathbf{n}}) A_k \int \frac{d^3\mathbf{k}}{(2\pi)^3} \frac{-i\mathbf{k} \cdot \hat{\mathbf{n}}}{k} \left(\frac{H_0 f_0}{ck} \right) W(kR) \delta(\mathbf{k}) \end{aligned} \quad (\text{A9})$$

and then use that with $\mathbf{x} = \chi \hat{\mathbf{n}}$, where χ the comoving distance, the dipole $-i\mathbf{k} \cdot \hat{\mathbf{n}}$ can be expressed as $-i\mathbf{k} \cdot \hat{\mathbf{n}} = (\partial e^{-i\mathbf{k} \cdot \chi \hat{\mathbf{n}}} / \partial \chi)|_{\chi=0}$. Now substituting the plane-wave expansion into equation (A9) we find

$$\begin{aligned} b_{1M} &= \int d^2\hat{\mathbf{n}} Y_{1M}^*(\hat{\mathbf{n}}) A_k \int \frac{d^3\mathbf{k}}{(2\pi)^3} \left(\frac{H_0 f_0}{ck} \right) W(kR) \delta(\mathbf{k}) \\ &\quad \times \frac{1}{k} \frac{\partial}{\partial \chi} \left[\sum_{\ell, m} (-i)^\ell 4\pi j_\ell(k\chi) Y_{\ell m}^*(\hat{\mathbf{k}}) Y_{\ell m}(\hat{\mathbf{n}}) \right]_{\chi=0} \\ &= (-i) 4\pi \int \frac{d^3\mathbf{k}}{(2\pi)^3} Y_{1M}^*(\hat{\mathbf{k}}) A_k \left(\frac{H_0 f_0}{ck} \right) W(kR) \delta(\mathbf{k}) \frac{1}{k} \frac{\partial j_1}{\partial \chi} \Big|_{\chi=0}, \end{aligned}$$

where in the second line we have used the orthogonality of spherical harmonics. Since $j_1(x) = x/3 + \mathcal{O}(x^3)$, the derivative with respect to χ , at $\chi = 0$, exactly evaluates to $k/3$; inserting $\delta(\mathbf{k}) = \mathcal{T}_\delta(k, z) \zeta(\mathbf{k})$, we finally get

$$b_{1M} = (-i) 4\pi \int \frac{d^3\mathbf{k}}{(2\pi)^3} Y_{1M}^*(\hat{\mathbf{k}}) \left[\frac{1}{3} A_k W(kR) \left(\frac{H_0 f_0}{ck} \right) \mathcal{T}_\delta(k) \right] \zeta(\mathbf{k}),$$

where $\mathcal{T}_\delta(k)$ is evaluated at $z = 0$. Note that b_Q does not appear here because \mathbf{v} is sourced by matter perturbations. Since this expression is in the form of equation (A1) we can immediately read off the

kinematic transfer function from the contents of the square brackets:

$$\Delta_1^k(k) = \frac{1}{3} A_k W(kR) \left(\frac{H_0 f_0}{ck} \right) \mathcal{T}_\delta(k). \quad (\text{A10})$$

Note that because we evaluate \mathbf{v} at $\mathbf{x} = 0$ the transfer function $\mathcal{T}_\delta(k)$ is simply evaluated at $z = 0$ and not integrated. Further note that to include source evolution, simply replace A_k with its average \bar{A}_k given by equation (25).

APPENDIX B: PIXELIZATION

We can also consider the effect of the pixelization on the theoretical power. At the field level, the pixelization of the number-count fluctuations is given by

$$\delta_{Q,i} = \int d^2 \hat{\mathbf{n}} W_i^{\text{pix}}(\hat{\mathbf{n}}) \delta_Q(\hat{\mathbf{n}}), \quad (\text{B1})$$

where $W_i^{\text{pix}}(\hat{\mathbf{n}})$ is the HEALPIX pixel window function for the i th pixel, which is equal to zero, unless $\hat{\mathbf{n}}$ falls within the i th pixel, in which case W_i^{pix} is equal to $1/\Omega_{\text{pix}}$, with Ω_{pix} being the pixel area. This window function is normalised, $\int d^2 \hat{\mathbf{n}} W_i^{\text{pix}}(\hat{\mathbf{n}}) = 1$, so that $\delta_{Q,i}$ is the average fluctuation in the i th pixel. Note that because the HEALPIX pixel shape varies azimuthally there is no global pixel window function that applies to all pixels. Provided a large enough N_{side} is chosen this is not really a problem: the differences between pixel window functions only becomes important when considering large ℓ , but this can always be remedied by choosing a larger N_{side} .

We will ignore the azimuthal variation in pixels, as is routinely done. Under this approximation pixelized fields are also statistically isotropic and the angular power spectrum of the pixelized field is $C_\ell^{\text{pix}} = (\bar{W}_\ell^{\text{pix}})^2 C_\ell$, where C_ℓ is the unpixelized power, and $\bar{W}_\ell^{\text{pix}}$ is the HEALPIX pixel-averaged window function (Górski et al. 2005). Since $\bar{W}_\ell^{\text{pix}} \leq 1$ there is a loss of power for all ℓ (more for larger ℓ). In this work $N_{\text{side}} = 64$ with which we find that $\bar{W}_\ell^{\text{pix}}$ is equal to unity to within 0.5% for $\ell = 0$ to $\ell = 20$. As this power loss is negligible we have thus ignored the effects of pixelization on the theoretical power.

APPENDIX C: DERIVATION OF $p(D)$

In this appendix we derive the probability distribution function $p(D)$ in both the full-sky and cut-sky regimes. The PDF in the former case is well known; it is the Maxwellian. In the latter case, considering an arbitrary symmetric Galactic plane cut (the details of which will be fixed in Appendix D1), we derive another long-tailed PDF, one that is suppressed relative to the Maxwellian. The calculation comes down to the marginalisation (14), which we evaluate through the moment generating function. The full-sky PDF is parametrised by σ_{kk} , σ_{cc} , and σ_{kc} ; whilst the cut-sky PDF is parametrised by $\sigma_{\text{k}_x \text{k}_x}$, $\sigma_{\text{k}_z \text{k}_z}$, $\sigma_{\text{c}_x \text{c}_x}$, $\sigma_{\text{c}_z \text{c}_z}$, $\sigma_{\text{k}_x \text{c}_x}$, and $\sigma_{\text{k}_z \text{c}_z}$ (these are, however, linearly related to those of the full sky). The calculation is based on geometrical considerations; no cosmological model needs to be assumed.

C1 Full sky

To set up the problem, construct the six-dimensional vector $\mathbf{X} = (\mathbf{d}_k, \mathbf{d}_c)^\top$, with $\mathbf{X} \sim \mathcal{N}(\mathbf{0}, \mathbf{C})$. By statistical isotropy only components along the same axis can be correlated (x - x , y - y , etc). Thus \mathbf{C}

can be written in block matrix form (13), with each block proportional to the 3×3 identity matrix, $\langle \mathbf{d}_X \mathbf{d}_Y^\top \rangle \propto \mathbf{I}_3$, with $X, Y \in \{k, c\}$. In particular, we have that the expected amplitude of the kinematic dipole is $D_k \equiv \langle \mathbf{d}_k^2 \rangle^{1/2} = \sqrt{3} \sigma_{\text{kk}}$, and the expected amplitude of the clustering dipole is $D_c \equiv \langle \mathbf{d}_c^2 \rangle^{1/2} = \sqrt{3} \sigma_{\text{cc}}$, where the root three is due to σ_{kk} and σ_{cc} being one-dimensional dispersions, while D_k and D_c is the total dispersion. Evaluating σ_{kk} , σ_{cc} , and σ_{kc} requires specifying a cosmological model, but these are simply related to the $\ell = 1$ multipole of certain angular power spectra by $\sigma_{\text{XY}}^2 = 3C_1^{\text{XY}}/(4\pi)$.

Though \mathbf{C} is a 6×6 matrix there are only three parameters needed to specify it (on account of isotropy). In analysing this matrix we find it convenient to therefore write it as a Kronecker product:

$$\mathbf{C} = \begin{pmatrix} \sigma_{\text{kk}}^2 & \sigma_{\text{kc}}^2 \\ \sigma_{\text{kc}}^2 & \sigma_{\text{cc}}^2 \end{pmatrix} \otimes \mathbf{I}_3, \quad \mathbf{C}^{-1} = \begin{pmatrix} \sigma_{\text{kk}}^2 & \sigma_{\text{kc}}^2 \\ \sigma_{\text{kc}}^2 & \sigma_{\text{cc}}^2 \end{pmatrix}^{-1} \otimes \mathbf{I}_3, \quad (\text{C1})$$

where \mathbf{I}_3 is the 3×3 identity matrix, and the inverse \mathbf{C}^{-1} is the Kronecker product of the inverse of the two matrices.⁵ Thus we see that the covariances in \mathbf{C} are essentially contained in a 2×2 matrix.

The square of the amplitude of the total dipole, $Y \equiv D^2 = |\mathbf{d}_k + \mathbf{d}_c|^2$, can be recast as the quadratic form

$$Y = \mathbf{X}^\top \mathbf{A} \mathbf{X}, \quad \mathbf{A} \equiv \begin{pmatrix} \mathbf{I}_3 & \mathbf{I}_3 \\ \mathbf{I}_3 & \mathbf{I}_3 \end{pmatrix} = \begin{pmatrix} 1 & 1 \\ 1 & 1 \end{pmatrix} \otimes \mathbf{I}_3, \quad (\text{C2})$$

where \mathbf{A} is a 6×6 symmetric matrix. The moment generating function $M_Y(t) \equiv \langle e^{tY} \rangle$ can be written using the ‘law of the unconscious statistician’ as

$$M_Y(t) \equiv \int dY e^{tY} p(Y) = \int d^6 \mathbf{X} e^{t \mathbf{X}^\top \mathbf{A} \mathbf{X}} p(\mathbf{X}), \quad (\text{C3})$$

i.e. in terms of the probability distribution of \mathbf{X} . Before we compute the second integral, we recall that $M_Y(-t)$ is the (unilateral) Laplace transform \mathcal{L} of the PDF $p(Y)$:

$$\mathcal{L}[p(Y)](t) \equiv \int_0^\infty dY e^{-tY} p(Y) = M_Y(-t). \quad (\text{C4})$$

Therefore, once the moment generating function is in hand, and the sign of its argument is flipped, we recover the PDF by simply taking the inverse Laplace transform:

$$p(Y) = \mathcal{L}^{-1}[M_Y(-t)](Y) \equiv \frac{1}{2\pi i} \int_{\gamma-i\infty}^{\gamma+i\infty} dt e^{tY} M_Y(-t). \quad (\text{C5})$$

(Here γ is some large, positive constant, chosen so that the poles lie to the left of it in the complex plane.) In practice, we will not have to perform such integrals as we can build the solution out of simpler, known transforms, by using the convolution properties of the Laplace transform.⁶

To evaluate the second integral in equation (C3), we note that it has the basic form of a Gaussian convolution; because one ‘Gaussian’ is without its normalisation factor, we find after some straightforward matrix algebra

$$M_Y(t) = \det(\mathbf{I}_6 - 2t\mathbf{A}\mathbf{C})^{-1/2} = \prod_{j=1}^6 \lambda_j^{-1/2}, \quad (\text{C6})$$

where in the second equality we have expressed the determinant in

⁵ $\mathbf{A}^{-1} = (\mathbf{B} \otimes \mathbf{C})^{-1} = \mathbf{B}^{-1} \otimes \mathbf{C}^{-1}$.

⁶ Perhaps the more obvious approach to obtain the PDF is to use the characteristic function $\phi_Y(t) \equiv M_Y(it)$ together with the Fourier transform. However, this proves slightly awkward, since $Y \geq 0$ forces us to consider a one-sided Fourier transform.

terms of the eigenvalues λ_j of $\mathbf{I}_6 - 2t\mathbf{AC}$. Now specialising to the case of statistical isotropy, we find that there are only two distinct eigenvalues, which we call λ_1 and λ_2 . To see this we exploit the properties of the Kronecker product: write $\mathbf{I}_6 = \mathbf{I}_2 \otimes \mathbf{I}_3$ and $\mathbf{AC} = \boldsymbol{\Sigma} \otimes \mathbf{I}_3$, with

$$\boldsymbol{\Sigma} \equiv \begin{pmatrix} 1 & 1 \\ 1 & 1 \end{pmatrix} \begin{pmatrix} \sigma_{kk}^2 & \sigma_{kc}^2 \\ \sigma_{kc}^2 & \sigma_{cc}^2 \end{pmatrix} = \begin{pmatrix} \sigma_{kk}^2 + \sigma_{kc}^2 & \sigma_{cc}^2 + \sigma_{kc}^2 \\ \sigma_{kk}^2 + \sigma_{kc}^2 & \sigma_{cc}^2 + \sigma_{kc}^2 \end{pmatrix}. \quad (\text{C7})$$

Because $\mathbf{I}_6 - 2t\mathbf{AC} = (\mathbf{I}_2 - 2t\boldsymbol{\Sigma}) \otimes \mathbf{I}_3$, there are two distinct eigenvalues (each having multiplicity three) corresponding to the 2×2 matrix $\mathbf{I}_2 - 2t\boldsymbol{\Sigma}$. The eigenvalues are $\lambda_1 = 1$ and $\lambda_2 = 1 - 2t\Delta^2$, with

$$\Delta^2 \equiv \sigma_{kk}^2 + 2\rho\sigma_{kk}\sigma_{cc} + \sigma_{cc}^2. \quad (\text{C8})$$

Therefore, we have simply that $M_Y(t) = (1 - 2t\Delta^2)^{-3/2}$, which can be seen to closely resemble the moment generating function of the generalised chi-squared distribution. As mentioned, the PDF is recovered by inverse Laplace transform of $M_Y(-t)$:⁷

$$p(Y) = \frac{1}{2\pi i} \int_{\gamma - i\infty}^{\gamma + i\infty} \frac{e^{tY} dt}{(1 + 2t\Delta^2)^{3/2}} = \frac{\sqrt{Y} e^{-Y/(2\Delta^2)}}{\sqrt{2\pi}\Delta^3}. \quad (\text{C9})$$

Finally, the distribution for the amplitude $D \equiv \sqrt{Y}$ is $p(D) = p(Y=D^2) |dY/dD|$, or, explicitly, after some algebra,

$$p(D) dD = \frac{4}{\sqrt{\pi}} \exp\left(-\frac{D^2}{2\Delta^2}\right) \frac{D^2}{2\Delta^2} \frac{dD}{\sqrt{2}\Delta}. \quad (\text{C10})$$

This PDF, a chi distribution with three degrees of freedom (or Maxwellian), has mean $\langle D \rangle = \sqrt{8/\pi}\Delta$ and variance $\langle D^2 \rangle = 3\Delta^2$. However, the variance is larger than might be expected from a standard Maxwellian due to cross terms ($\sigma_{k_x c_x}^2, \sigma_{k_z c_z}^2$, etc).

C2 Cut sky

The Galactic plane cut, described later in Appendix D, has the effect of identifying a preferred direction, i.e. along the z -axis (where the z -axis is orthogonal to the Galactic plane). Because of this the covariance now takes the form

$$\mathbf{C} = \begin{pmatrix} \sigma_{k_x k_x}^2 & 0 & 0 & \sigma_{k_x c_x}^2 & 0 & 0 \\ 0 & \sigma_{k_x k_x}^2 & 0 & 0 & \sigma_{k_x c_x}^2 & 0 \\ 0 & 0 & \sigma_{k_z k_z}^2 & 0 & 0 & \sigma_{k_z c_z}^2 \\ \sigma_{k_x c_x}^2 & 0 & 0 & \sigma_{c_x c_x}^2 & 0 & 0 \\ 0 & \sigma_{k_x c_x}^2 & 0 & 0 & \sigma_{c_x c_x}^2 & 0 \\ 0 & 0 & \sigma_{k_z c_z}^2 & 0 & 0 & \sigma_{c_z c_z}^2 \end{pmatrix}. \quad (\text{C11})$$

Notice now that each 3×3 block matrix is no longer proportional to the identity matrix, so cannot be written as a Kronecker product. In particular, we now see that the dispersions of the x - and y -components differ from that of the z -component. Because of this $\sigma_{c_x c_x}^2 = \sigma_{c_y c_y}^2 \neq \sigma_{c_z c_z}^2$ and $\sigma_{k_x k_x}^2 = \sigma_{k_y k_y}^2 \neq \sigma_{k_z k_z}^2$; similarly, for the cross-terms

⁷ The integral can be done with help of the convolution theorem, which says that a product of moment generating functions corresponds to the convolution of their individual PDFs. Thus we write $(1 - 2t\Delta^2)^{-3/2} = \prod_{j=1}^3 (1 - 2t\Delta_j^2)^{-1/2}$, and note that the chi-squared distribution with one degree of freedom has a moment generating function $(1 - 2t\Delta^2)^{-1/2}$. Then the PDF corresponding to $M_Y(t)$ is the convolution $p(Y) = p_x * p_y * p_z$ of three such chi-squared distributions, which yields another chi-squared distribution but with three degrees of freedom.

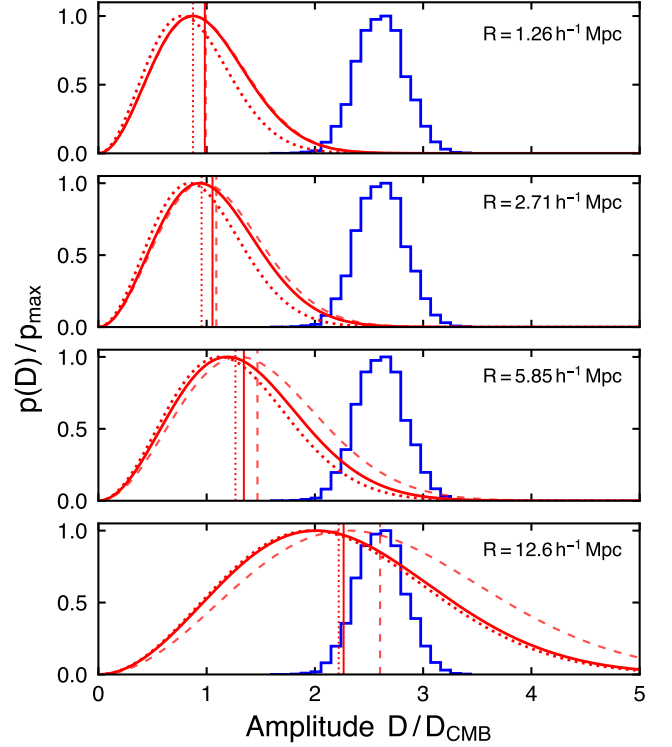


Figure C1. As for Fig. 4 but on the full sky ($f_{\text{sky}} = 1$). The probability distribution is simply the Maxwellian (C10) with dispersions given by equations (20). The main point here is that without the mask larger values of D are more probable compared with the case of including the mask

$\sigma_{k_x c_x}^2 = \sigma_{k_y c_y}^2 \neq \sigma_{k_z c_z}^2$. The probability distribution $p(D)$ is now given in terms of six independent quantities, $\sigma_{k_x k_x}^2, \sigma_{k_z k_z}^2, \sigma_{c_x c_x}^2, \sigma_{c_z c_z}^2, \sigma_{k_x c_x}^2$, and $\sigma_{k_z c_z}^2$.

We still have azimuthal symmetry (rotations about the z -axis), and this is reflected in the x and y components. This is also seen in the multiplicity of the eigenvalues, which are now $\lambda_1 = 1 - 2t\Delta_z^2$ (multiplicity one), $\lambda_2 = 1 - 2t\Delta_x^2$ (multiplicity two), and $\lambda_3 = 1$ (multiplicity three), where Δ_x^2 and Δ_z^2 are given by equations (16a) and (16b), respectively. With respect to the Galactic plane, we decompose into transverse (x and y) and longitudinal components (z), labelled collectively by ‘ \perp ’ and ‘ \parallel ’, respectively.

We now have two distinct t -dependent eigenvalues (where previously in the full-sky case there was only one), thus producing one additional pole in the moment generating function:

$$M_Y(t) = M_{Y_\perp}(t) M_{Y_\parallel}(t), \quad (\text{C12})$$

with $M_{Y_\perp}(t) \equiv M_{Y_x}(t) M_{Y_y}(t)$, $M_{Y_x}(t) = M_{Y_y}(t) = (1 - 2t\Delta_x^2)^{-1/2}$, and $M_{Y_\parallel}(t) = M_{Y_z}(t) = (1 - 2t\Delta_z^2)^{-1/2}$ (these can be found by considering the eigenvalues of the covariance matrix (C11)). The PDFs of each of these constituent moment generating functions are obtained by the following inverse Laplace transforms:

$$p_\perp(Y) = \mathcal{L}^{-1}[M_{Y_\perp}(-t)](Y) = \frac{e^{-Y/(2\Delta_x^2)}}{2\Delta_x^2}, \quad (\text{C13a})$$

$$p_\parallel(Y) = \mathcal{L}^{-1}[M_{Y_\parallel}(-t)](Y) = \frac{e^{-Y/(2\Delta_z^2)}}{(2\pi Y \Delta_z^2)^{1/2}}. \quad (\text{C13b})$$

By the convolution theorem of the unilateral Laplace trans-

form, the PDF of the product of moment generating functions $p(Y) = \mathcal{L}^{-1}[M_{Y_\perp}(-t)M_{Y_\parallel}(-t)]$ is equal to the convolution $\mathcal{L}^{-1}[M_{Y_\perp}(-t)] * \mathcal{L}^{-1}[M_{Y_\parallel}(-t)]$, which evaluates to

$$p(Y) = \int_0^Y dY' p_\perp(Y - Y') p_\parallel(Y') = \frac{1}{\sqrt{\varepsilon}} \operatorname{erf}\left(\frac{\varepsilon Y}{2\Delta_z^2}\right) \frac{e^{-Y/(2\Delta_x^2)}}{2\Delta_x^2},$$

where $\varepsilon \equiv 1 - \Delta_z^2/\Delta_x^2$ gives the ‘eccentricity’ of the ellipsoid spanned by the eigenvectors. The use of the error function in the foregoing equation is valid for $\varepsilon > 0$; for $\varepsilon < 0$, which is the case for the Galactic plane cut, we have instead

$$p(Y) = \frac{2}{\sqrt{\pi|\varepsilon|}} e^{|\varepsilon|Y/(2\Delta_z^2)} F\left(\frac{\sqrt{|\varepsilon|}\sqrt{Y}}{\sqrt{2}\Delta_z}\right) \frac{e^{-Y/(2\Delta_x^2)}}{2\Delta_x^2}, \quad (\text{C14})$$

where $F(x) \equiv e^{-x^2} \int_0^x dt e^{t^2}$ is the Dawson function (NIST DLMF 2023, 7.2.5).

The probability distribution of the amplitude $D = \sqrt{Y}$, in the presence of a Galactic plane cut, is now obtained easily from $p(D) = p(Y = D^2) |dY/dD|$; it is

$$p(D) dD = \frac{2D dD}{\sqrt{\pi|\varepsilon|\Delta_x^2}} F\left(\frac{\sqrt{|\varepsilon|}D}{\sqrt{2}\Delta_z}\right) \exp\left(-\frac{D^2}{2\Delta_x^2}\right), \quad (\text{C15})$$

where we have used that $|\varepsilon| = \Delta_z^2/\Delta_x^2 - 1 > 0$, since for us $\varepsilon < 0$. We can bring equation (C15) into a form more closely resembling the full-sky case (i.e. the Maxwell–Boltzmann distribution) by using $\Delta_x^2 = \Delta_z^2/(1 - \varepsilon)$ to rewrite it in terms of Δ_z and ε . After some algebra, and after defining the function $\mathcal{F}(x) \equiv F(x)/x$, we arrive at our final form [cf. equation (C10)]:

$$p(D) dD = (1 - \varepsilon) \mathcal{F}\left(\frac{\sqrt{|\varepsilon|}D}{\sqrt{2}\Delta_z}\right) \frac{4}{\sqrt{\pi}} \exp\left(-\frac{D^2}{2\Delta_z^2}\right) \frac{D^2}{2\Delta_z^2} \frac{dD}{\sqrt{2}\Delta_z}. \quad (\text{C16})$$

This is equation (15) in the main text. As a consistency check, it is easy to verify using $\mathcal{F}(a\sqrt{\varepsilon}) \rightarrow 1$, as $\varepsilon \rightarrow 0$, that the full-sky expression (C10) derived in the previous section is recovered in the limit $\varepsilon \rightarrow 0$. This is the special case of statistical isotropy, for which $\Delta_x = \Delta_y = \Delta_z$.

The first three moments of the PDF (C16) are

$$\langle D \rangle = \sqrt{\frac{2}{\pi}} \left[\Delta_z + \Delta_x \frac{\operatorname{arcsinh}(\sqrt{|\varepsilon|})}{\sqrt{|\varepsilon|}} \right], \quad (\text{C17a})$$

$$\langle D^2 \rangle = \Delta_z^2 + 2\Delta_x^2, \quad (\text{C17b})$$

$$\langle D^3 \rangle = \sqrt{\frac{2}{\pi}} \left[2\Delta_z^3 + 3\Delta_z\Delta_x^2 + 3\Delta_x^3 \frac{\operatorname{arcsinh}(\sqrt{|\varepsilon|})}{\sqrt{|\varepsilon|}} \right]. \quad (\text{C17c})$$

In the limit $\varepsilon \rightarrow 0$, these recover the usual moments of the Maxwell–Boltzmann distribution, i.e. $\langle D \rangle = \sqrt{8/\pi}\Delta$, $\langle D^2 \rangle = 3\Delta^2$, and $\langle D^3 \rangle = 4\sqrt{8/\pi}\Delta^3$, with $\Delta = \Delta_x = \Delta_y = \Delta_z$.

APPENDIX D: DIPOLE STATISTICS ON THE CUT SKY

In order to compare the dipole estimate with the theoretical value we will convolve the full-sky predictions with the mask.

D1 Galactic plane cut

We make a symmetric cut about the Galactic plane, excluding a central region $|b| \leq b_{\text{cut}}$. Here $b_{\text{cut}} = 30^\circ$, as in S21. This conservative

cut removes half of the sky ($f_{\text{sky}} = 0.5$). Since the additional masks (accounting for poor-quality photometry, image artefacts, etc) covers merely 1.2% of the sky we will ignore their effect on the power, which principally affects the small angular scales. We will thus apply to the number-count field $dN/d\Omega(\hat{\mathbf{n}})$ the following mask:

$$\mathcal{W}(\vartheta) = \begin{cases} 0, & \vartheta_- \leq \vartheta \leq \vartheta_+, \\ 1, & \text{otherwise,} \end{cases} \quad (\text{D1})$$

where $\vartheta_\pm = \pi/2 \pm b_{\text{cut}}$. In terms of the Heaviside step function Θ , this can also be written as

$$\mathcal{W}(\hat{\mathbf{n}}) = \Theta(\hat{\mathbf{n}} \cdot \hat{\mathbf{z}} - \mu_-) + \Theta(\mu_+ - \hat{\mathbf{n}} \cdot \hat{\mathbf{z}}), \quad (\text{D2})$$

with $\mu_\pm = \cos \vartheta_\pm$, and where the first and second term selects the northern and southern caps, respectively. Because $\mathcal{W}(\hat{\mathbf{n}})$ possesses azimuthal symmetry, its spherical harmonic expansion is given purely in terms of the zonal modes ($m = 0$): $\mathcal{W}(\vartheta) = \sum_\ell \mathcal{W}_{\ell 0} Y_{\ell 0}(\vartheta)$. Furthermore, because $\mathcal{W}(\hat{\mathbf{n}})$ is parity symmetric, $\mathcal{W}_{\ell m} = \int d^2\hat{\mathbf{n}} \mathcal{W}(\hat{\mathbf{n}}) Y_{\ell m}^*(\hat{\mathbf{n}})$ is equal to zero for odd ℓ ; for even ℓ these coefficients are non-zero and are given by (Dahlen & Simons 2008)

$$\mathcal{W}_{\ell m} = 2\delta_{m0}^K \sqrt{\frac{\pi}{2\ell+1}} [\mathcal{L}_{\ell-1}(\mu_-) - \mathcal{L}_{\ell+1}(\mu_-)] \quad (\text{even } \ell), \quad (\text{D3})$$

where $\mathcal{L}_\ell(\mu)$ is the Legendre polynomial of degree ℓ [note $\mathcal{L}_{-1}(\mu) \equiv 1$]. With $b_{\text{cut}} = 30^\circ$ we have for the first five non-zero coefficients $\mathcal{W}_{00} \approx 1.77245$, $\mathcal{W}_{20} \approx 1.48625$, $\mathcal{W}_{40} \approx -0.623128$, $\mathcal{W}_{60} \approx -0.131059$, and $\mathcal{W}_{80} \approx 0.422182$.

D2 Mode coupling

A cut on the sky breaks statistical isotropy. In harmonic space this implies that the covariance matrix of $a_{\ell m}$ ’s can have off-diagonal components, i.e. we no longer have that $\langle a_{\ell m} b_{\ell' m'}^* \rangle = C_\ell \delta_{\ell\ell'}^K \delta_{mm'}^K$. Now, $a_{\ell m}$ with different ℓ or m may be correlated.

We now apply the mask $\mathcal{W}(\hat{\mathbf{n}})$ to the number-count field $dN/d\Omega(\hat{\mathbf{n}}) \rightarrow \mathcal{W}(\hat{\mathbf{n}})dN/d\Omega(\hat{\mathbf{n}})$. Denoting by $\tilde{a}_{\ell m}$ and $\tilde{b}_{\ell m}$ the coefficients of the masked fields $\mathcal{W}(\hat{\mathbf{n}})\delta_Q(\hat{\mathbf{n}})$ and $\mathcal{W}(\hat{\mathbf{n}})(\mathbf{d}_k \cdot \hat{\mathbf{n}})$, respectively, it can be shown using the properties of spherical harmonics that we now have a linear coupling of the underlying $a_{\ell m}$ and $b_{\ell m}$ (Peebles 1980):

$$\tilde{a}_{\ell m} = \sum_{\ell' m'} \mathcal{A}_{\ell m \ell' m'} a_{\ell' m'}, \quad \tilde{b}_{\ell m} = \sum_{\ell' m'} \mathcal{B}_{\ell m \ell' m'} b_{\ell' m'}. \quad (\text{D4})$$

Here $\mathcal{A}_{\ell m \ell' m'}$ is a harmonic kernel which is determined by the window function $\mathcal{W}(\hat{\mathbf{n}})$; for a general $\mathcal{W}(\hat{\mathbf{n}}) = \sum_{\ell, m} \mathcal{W}_{\ell m} Y_{\ell m}(\hat{\mathbf{n}})$, it is given by (Hivon et al. 2002)

$$\begin{aligned} \mathcal{A}_{\ell_1 m_1 \ell_2 m_2} &\equiv \sum_{\ell_3 m_3} \mathcal{W}_{\ell_3 m_3} \int d^2\hat{\mathbf{n}} Y_{\ell_1 m_1}(\hat{\mathbf{n}}) Y_{\ell_2 m_2}^*(\hat{\mathbf{n}}) Y_{\ell_3 m_3}(\hat{\mathbf{n}}) \\ &= (-1)^{m_2} \sum_{\ell_3 m_3} \mathcal{W}_{\ell_3 m_3} \left[\frac{(2\ell_1 + 1)(2\ell_2 + 1)(2\ell_3 + 1)}{4\pi} \right]^{1/2} \\ &\quad \times \begin{pmatrix} \ell_1 & \ell_2 & \ell_3 \\ 0 & 0 & 0 \end{pmatrix} \begin{pmatrix} \ell_1 & \ell_2 & \ell_3 \\ m_1 & -m_2 & m_3 \end{pmatrix}, \end{aligned} \quad (\text{D5})$$

where the arrays are Wigner $3j$ symbols, coefficients that encode selection rules for the allowed combinations of ℓ ’s and m ’s. Using that $\mathcal{A}_{\ell m \ell' m'} = \mathcal{A}_{\ell m \ell' m} \delta_{mm'}^K$ (by azimuthal symmetry), and $\mathcal{A}_{\ell m \ell' m'}^* = \mathcal{A}_{\ell m \ell' m'}$ (because $\mathcal{W}_{\ell 0}^* = \mathcal{W}_{\ell 0}$), we have for two arbitrary fields, each with azimuthally-symmetric masks (which need

not be identical),

$$\begin{aligned} \langle \tilde{a}_{\ell_1 m_1} \tilde{b}_{\ell_2 m_2}^* \rangle &= \sum_{\ell'_1, \ell'_2, m'_1, m'_2} \mathcal{A}_{\ell_1 m_1 \ell'_1 m'_1} \mathcal{B}_{\ell_2 m_2 \ell'_2 m'_2}^* \langle a_{\ell'_1 m'_1} b_{\ell'_2 m'_2}^* \rangle \\ &= \delta_{m_1 m_2}^K \sum_{\ell} \mathcal{A}_{\ell_1 m_1 \ell m_1} \mathcal{B}_{\ell_2 m_2 \ell m_1} C_{\ell}. \end{aligned} \quad (\text{D6})$$

In our case – with $\tilde{a}_{\ell m}$ corresponding to the clustering field and $\tilde{b}_{\ell m}$ corresponding to the kinematic field – we only need to consider $\ell_1 = \ell_2 = 1$, with identical mask applied to both fields ($\mathcal{A} = \mathcal{B}$). In terms of the underlying power spectra we have

$$\langle \tilde{a}_{1m} \tilde{b}_{1m'}^* \rangle = \delta_{mm'}^K |\mathcal{A}_{1m1m}|^2 C_1^{\text{kc}}, \quad (\text{D7a})$$

$$\langle \tilde{a}_{1m} \tilde{a}_{1m'}^* \rangle = \delta_{mm'}^K \sum_{\ell \text{ odd}} |\mathcal{A}_{1m\ell m}|^2 C_{\ell}^{\text{cc}}, \quad (\text{D7b})$$

$$\langle \tilde{b}_{1m} \tilde{b}_{1m'}^* \rangle = \delta_{mm'}^K |\mathcal{A}_{1m1m}|^2 C_1^{\text{kk}}, \quad (\text{D7c})$$

where only odd ℓ need to be considered because of the selection rules of Wigner $3j$ symbols in equation (D5). Note that no off-diagonal entries are induced in the covariance matrix in harmonic space. However, in Cartesian space the covariance matrix is no longer proportional to the identity matrix (although it remains diagonal). Though we will no longer have spherical symmetry we still have azimuthal symmetry.

For $b_{\text{cut}} = 30^\circ$, the first three coupling coefficients are $|\mathcal{A}_{1010}|^2 \approx 0.76563$, $|\mathcal{A}_{1030}|^2 \approx 0.046143$, and $|\mathcal{A}_{1050}|^2 \approx 0.034272$. Also $|\mathcal{A}_{1111}|^2 \approx 0.0976563$, $|\mathcal{A}_{1131}|^2 \approx 0.155731$, and $|\mathcal{A}_{1151}|^2 \approx 0.00955939$. These values indicate a substantial loss of power for the x - and y -components of the dipole.

D3 Dipole dispersions

We now need to relate the statistics in harmonic space back to the statistics in Cartesian space. To facilitate this it will be convenient to define the complex-valued vectors $\tilde{\mathbf{a}}_1 \equiv (\tilde{a}_{1-1}, \tilde{a}_{11}, \tilde{a}_{10})^\top$ and $\tilde{\mathbf{b}}_1 \equiv (\tilde{b}_{1-1}, \tilde{b}_{11}, \tilde{b}_{10})^\top$. We then have the following linear relation between the Cartesian- and harmonic-space dipoles:

$$\mathbf{d}_c = \sqrt{\frac{3}{4\pi}} \mathbf{U}^\dagger \tilde{\mathbf{a}}_1, \quad \mathbf{d}_k = \sqrt{\frac{3}{4\pi}} \mathbf{U}^\dagger \tilde{\mathbf{b}}_1, \quad (\text{D8})$$

where the tilde indicates coefficients of masked fields, and \mathbf{U} is given by equation (A4). With these relations we can express the covariances of these vectors, $\langle \mathbf{d}_X \mathbf{d}_Y^\top \rangle$, in terms of the underlying power spectra:

$$\begin{aligned} \langle \mathbf{d}_k \mathbf{d}_k^\top \rangle &= \frac{3}{4\pi} \mathbf{U}^\dagger \langle \tilde{\mathbf{b}}_1 \tilde{\mathbf{b}}_1^\dagger \rangle \mathbf{U} \\ &= \text{diag}(|\mathcal{A}_{1111}|^2, |\mathcal{A}_{1111}|^2, |\mathcal{A}_{1010}|^2) \frac{3C_1^{\text{kk}}}{4\pi}, \end{aligned} \quad (\text{D9a})$$

$$\begin{aligned} \langle \mathbf{d}_k \mathbf{d}_c^\top \rangle &= \frac{3}{4\pi} \mathbf{U}^\dagger \langle \tilde{\mathbf{b}}_1 \tilde{\mathbf{a}}_1^\dagger \rangle \mathbf{U} \\ &= \text{diag}(|\mathcal{A}_{1111}|^2, |\mathcal{A}_{1111}|^2, |\mathcal{A}_{1010}|^2) \frac{3C_1^{\text{kc}}}{4\pi}, \end{aligned} \quad (\text{D9b})$$

$$\begin{aligned} \langle \mathbf{d}_c \mathbf{d}_c^\top \rangle &= \frac{3}{4\pi} \mathbf{U}^\dagger \langle \tilde{\mathbf{a}}_1 \tilde{\mathbf{a}}_1^\dagger \rangle \mathbf{U} \\ &= \sum_{\ell \text{ odd}} \text{diag}(|\mathcal{A}_{11\ell 1}|^2, |\mathcal{A}_{11\ell 1}|^2, |\mathcal{A}_{10\ell 0}|^2) \frac{3C_{\ell}^{\text{cc}}}{4\pi}, \end{aligned} \quad (\text{D9c})$$

The block-matrix form of the 6×6 cut-sky covariance (C11) is constructed out of these 3×3 covariances. The first matrix $\langle \mathbf{d}_k \mathbf{d}_k^\top \rangle \propto \mathbf{I}_3$ is unchanged from before; the second and third matrices are diagonal but have different dispersions from before. For instance, the dispersion of the z -component is proportional to $\langle |\tilde{a}_{10}|^2 \rangle = \sum_{\ell} |\mathcal{A}_{10\ell 0}|^2 C_{\ell}$, while the x - and y -components both

have dispersions proportional to $\langle |\tilde{a}_{11}|^2 \rangle = \sum_{\ell} |\mathcal{A}_{11\ell 1}|^2 C_{\ell}$, with $\mathcal{A}_{11\ell 1} \neq \mathcal{A}_{10\ell 0}$.

We can relate the harmonic form to the dispersions in the cut-sky covariance matrix (C11) as follows. Again, because of azimuthal symmetry, we recall that the dispersions for the x - and y -components are equal (though modified from before), e.g. $\sigma_{c_x c_x}^2 = \sigma_{c_y c_y}^2$, $\sigma_{k_x c_x}^2 = \sigma_{k_y c_y}^2$, etc. The new dispersions, in terms of the spectra, now read

$$\begin{aligned} \sigma_{k_x k_x}^2 &= \frac{3}{4\pi} |\mathcal{A}_{1111}|^2 C_1^{\text{kk}}, & \sigma_{k_z k_z}^2 &= \frac{3}{4\pi} |\mathcal{A}_{1010}|^2 C_1^{\text{kk}}, \\ \sigma_{c_x c_x}^2 &= \frac{3}{4\pi} \sum_{\ell \text{ odd}} |\mathcal{A}_{11\ell 1}|^2 C_{\ell}^{\text{cc}}, & \sigma_{c_z c_z}^2 &= \frac{3}{4\pi} \sum_{\ell \text{ odd}} |\mathcal{A}_{10\ell 0}|^2 C_{\ell}^{\text{cc}}, \\ \sigma_{k_x c_x}^2 &= \frac{3}{4\pi} |\mathcal{A}_{1111}|^2 C_1^{\text{kc}}, & \sigma_{k_z c_z}^2 &= \frac{3}{4\pi} |\mathcal{A}_{1010}|^2 C_1^{\text{kc}}, \end{aligned}$$

where C_{ℓ}^{XY} is given by equation (17). The dispersions related to the total dipole are given in terms of these by equations (16a) and (16b). For Λ CDM, though we have $C_{\ell}^{\text{cc}} > C_1^{\text{cc}}$, for $\ell \geq 2$, the leakage of power into the dipole is not enough to overcome the loss of power across all ℓ , e.g. $\sigma_{k_z k_z}^2 = |\mathcal{A}_{1010}|^2 \sigma_{\text{kk}}^2 \approx 0.77 \sigma_{\text{kk}}^2$, a 23% loss of kinematic dipole power. Because of this we find that we only need to sum up the first few odd multipoles to attain convergence (here we take $\ell_{\text{max}} = 9$).

This paper has been typeset from a $\text{\TeX}/\text{\LaTeX}$ file prepared by the author.